Matter

CellPress

Article

Supramolecular filaments for concurrent ACE2 docking and enzymatic activity silencing enable coronavirus capture and infection prevention

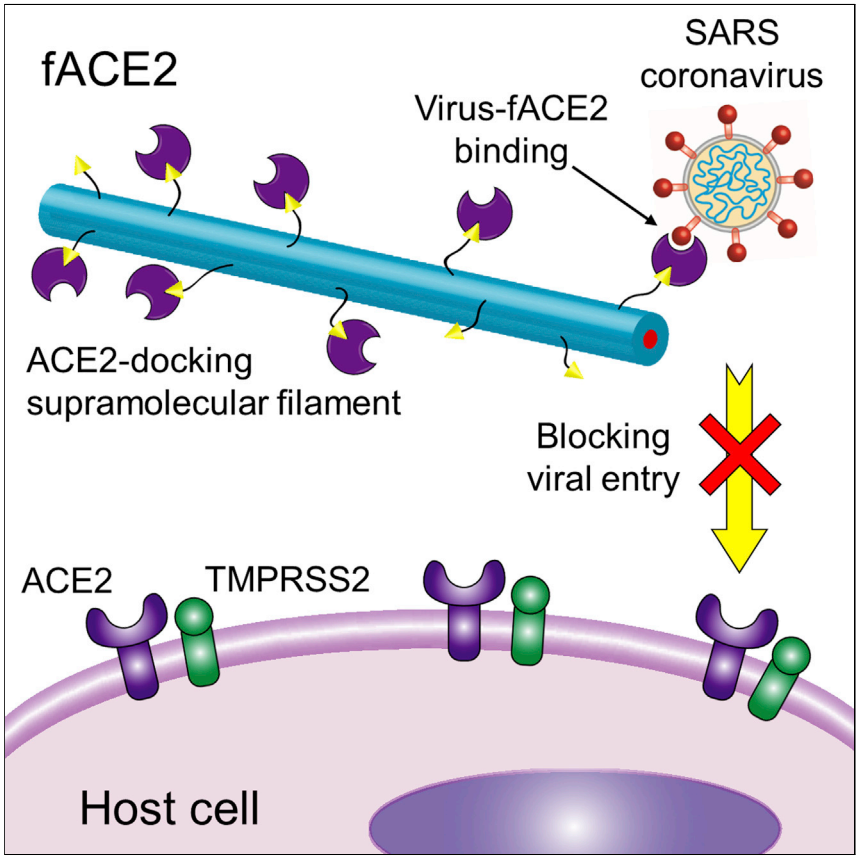

Peptide-based supramolecular filaments were designed to specifically bind and immobilize decoy ACE2 on their surface through enzyme-substrate interactions, which facilitated delivery of the protein in respirable aerosols. This docking strategy afforded structural and functional preservation of ACE2, leading to prolonged inhibition of SARS coronavirus infection *in vivo*. These protein-docking supramolecular filaments represent a new platform to deliver therapeutic proteins in inhalable aerosols for treatment of infectious and other human diseases.

Demonstrate
Proof-of-concept of performance with intended application/response

Caleb F. Anderson, Qiong Wang, David Stern, ..., Cory F. Brayton, Hongpeng Jia, Honggang Cui

hjia4@jhmi.edu (H.J.)
hcui6@jhu.edu (H.C.)

Highlights

Supramolecular filaments dock ACE2 via enzyme-substrate complexation

Docking affords delivery and preservation of ACE2 in inhalable aerosols

Filaments enhance and extend inhibition of viral entry of SARS coronaviruses

Anderson et al., Matter 6, 583–604
February 1, 2023
https://doi.org/10.1016/j.matt.2022.11.027

Matter

CellPress

Article

Supramolecular filaments for concurrent ACE2 docking and enzymatic activity silencing enable coronavirus capture and infection prevention

Caleb F. Anderson,[1,2] Qiong Wang,[3] David Stern,[1,2] Elissa K. Leonard,[4] Boran Sun,[1,2] Kyle J. Fergie,[1,2] Chang-yong Choi,[3] Jamie B. Spangler,[1,4,5,7] Jason Villano,[8] Andrew Pekosz,[7,8] Cory F. Brayton,[8] Hongpeng Jia,[3,*] and Honggang Cui[1,2,5,6,9,*]

SUMMARY

Coronaviruses have historically precipitated global pandemics of severe acute respiratory syndrome (SARS) into devastating public health crises. Despite the virus's rapid rate of mutation, all SARS coronavirus 2 (SARS-CoV-2) variants are known to gain entry into host cells primarily through complexation with angiotensin-converting enzyme 2 (ACE2). Although ACE2 has potential as a druggable decoy to block viral entry, its clinical use is complicated by its essential biological role as a carboxypeptidase and hindered by its structural and chemical instability. Here we designed supramolecular filaments, called fACE2, that can silence ACE2's enzymatic activity and immobilize ACE2 to their surface through enzyme-substrate complexation. This docking strategy enables ACE2 to be effectively delivered in inhalable aerosols and improves its structural stability and functional preservation. fACE2 exhibits enhanced and prolonged inhibition of viral entry compared with ACE2 alone while mitigating lung injury *in vivo*.

INTRODUCTION

Numerous infectious diseases are contracted primarily via deposition of bacteria and/or viruses into the respiratory tract, including tuberculosis, influenza, and, recently, coronavirus disease 2019 (COVID-19). The global COVID-19 pandemic, caused by the novel severe acute respiratory syndrome coronavirus 2 (SARS-CoV-2; also known as 2019-nCoV), has progressed into a grievous public health crisis with over 460 million confirmed cases of the disease and 6 million deaths worldwide as of March 15, 2022.[1,2] Therefore, it continues to be of paramount importance to rapidly develop effective vaccine or therapeutic strategies to address the ongoing COVID-19 pandemic and potential future epidemics.[3] Although the US Food and Drug Administration (FDA) has granted full approval and emergency use authorization for some vaccine formulations and disease treatments,[4,5] the virus continues to spread rapidly and subsequently mutate, leading to emergence of variants of concern (VOCs) of SARS-CoV-2; exactly how these prophylactic and therapeutic agents will handle these and future mutations alongside new viruses is subject of an evolving investigation.[6–9] Although SARS-CoVs may mutate, these viruses predominantly function by their S protein binding to the cognate receptor angiotensin-converting enzyme 2 (ACE2), which is the first step for viral entry, replication, and transmission; therefore, ACE2 is a logical druggable target for combating current and future CoVs.[10–13] ACE2 exists in membrane-bound and soluble forms, where

PROGRESS AND POTENTIAL

The structural and functional instability of therapeutic proteins represents a big challenge for their effective delivery and eventual use in the clinic. This work evidences enhanced deposition and retention of therapeutic proteins in the lungs through their complexation with high-affinity supramolecular filaments. Our results suggest that supramolecular filaments not only allow facile incorporation of peptide-based substrates on their surfaces for binding and delivering therapeutic proteins through enzyme-substrate interactions but also provide a means of preserving the proteins' structure and function as the filament and cargo endure harsh interfacial forces during aerosol formation. This eventually led to prolonged inhibition of coronavirus infection *in vitro* and *in vivo*. The materials showcased here possess high translational potential to curb coronavirus infections and establish a new platform for inhalable delivery of protein therapeutic agents for other human diseases.

both share the same enzymatic and viral binding functionalities, but only membrane-bound ACE2 is believed to facilitate viral entry and consequent infectivity.[14,15] Therefore, soluble ACE2 can serve as a decoy receptor by binding to the S protein on the virus surface and block the mechanism of viral entry into host cells, making soluble ACE2 an attractive candidate for preventing CoV infection.[16–18]

Clinical translation of soluble ACE2 remains challenging in the context of SARS-related CoV infections because the enzyme is unstable and can quickly degrade, especially in an inflammatory setting.[19] An additional hurdle exists in delivery of therapeutic ACE2 to its target site (in the case of COVID-19, the airway and the lungs), where efficacy suffers from its short half-life and lack of active transport mechanisms from the circulation into the epithelial lining fluid of the lungs when delivered by intravenous injection.[20–22] Recent advances in nanomaterials have yielded carriers of decoy ACE2 that help address these challenges; for instance, development of cell membrane-derived nanoparticles that curb SARS-CoV-2 infectivity in lung tissue.[23–25] However, given the essential roles of ACE2, as a carboxypeptidase, in regulating cardiovascular function, hypertension, and innate immune systems, it remains unclear whether delivery of enzymatically active ACE2 would lead to unknown mid- to long-term complications to the host.[20] In this context, we harness the multivalent nature of ACE2, where the enzyme's proteolytic activity and viral receptor properties are independent and non-interfering (sites highlighted in the ACE2 structure in Figure 1A),[20] to silence ACE2's enzymatic function and display the decoy receptors on the surface of peptide-based supramolecular filamentous nanostructures via enzyme-substrate complexation. We designed peptide amphiphiles (PAs), a class of molecular building units capable of spontaneously associating in aqueous solution to form one-dimensional supramolecular biomaterials,[26–29] to present a peptide ligand/inhibitor capable of binding to the active proteolytic site of ACE2 on the filament surface. Peptide-based supramolecular materials have been designed to facilitate various supramolecular interactions to immobilize proteins on structure surfaces to enhance protein stability and delivery[30–34] and could be highly advantageous as carriers for decoy ACE2. In addition to being deliverable in aerosols,[35,36] the charged surface and high aspect ratio likely aid deposition and retention atop the mucus layer coating the lung epithelium while mitigating cellular internalization, extending the availability of ACE2 at its target site while also mitigating potential hazardous contact of captured virus with host cells.[37–42] In this work, we developed ACE2-docking supramolecular filaments that effectively bind ACE2 through enzyme-substrate complexation to inhibit its enzymatic activity and demonstrate the decoy function of ACE2 to effectively capture SARS-CoVs and attenuate viral infectivity *in vivo*.

RESULTS AND DISCUSSION

Design and assembly of ACE2-docking supramolecular filaments

When designing our supramolecular filaments, we aimed to leverage the carboxypeptidase activity of ACE2 to allow enzyme docking and presentation of the SARS-CoV-2 S protein receptor-binding domain (RBD) binding site of ACE2 at the filament surface. These two sites on ACE2 are distinct and non-interfering (the ACE2 structure with these sites highlighted is shown in Figure 1A).[11,13,43] With this rationale, we selected a known potent peptide inhibitor of ACE2 enzymatic activity to incorporate into the design of an ACE2-binding PA, called Ligand (the molecular design is highlighted in Figures 1B and S1), and paired this PA with another self-assembling constituent of the filaments, a filler PA, called Filler (the molecular design is shown in Figures 1B and S2), which serves to modulate the distribution density of

[1]Department of Chemical and Biomolecular Engineering, Johns Hopkins University, Baltimore, MD 21218, USA

[2]Institute for NanoBioTechnology, Johns Hopkins University, Baltimore, MD 21218, USA

[3]Division of Pediatric Surgery, Department of Surgery, Johns Hopkins University School of Medicine, Baltimore, MD 21205, USA

[4]Department of Biomedical Engineering, Johns Hopkins University School of Medicine, Baltimore, MD 21205, USA

[5]Department of Oncology and Sidney Kimmel Comprehensive Cancer Center, Johns Hopkins University School of Medicine, Baltimore, MD 21205, USA

[6]Center for Nanomedicine, The Wilmer Eye Institute, Johns Hopkins University School of Medicine, Baltimore, MD 21231, USA

[7]Department of Molecular Microbiology and Immunology, The Johns Hopkins Bloomberg School of Public Health, Baltimore, MD 21205, USA

[8]Molecular and Comparative Pathobiology, The Johns Hopkins School of Medicine, Baltimore, MD 21205, USA

[9]Lead contact

*Correspondence: hjia4@jhmi.edu (H.J.), hcui6@jhu.edu (H.C.)

https://doi.org/10.1016/j.matt.2022.11.027

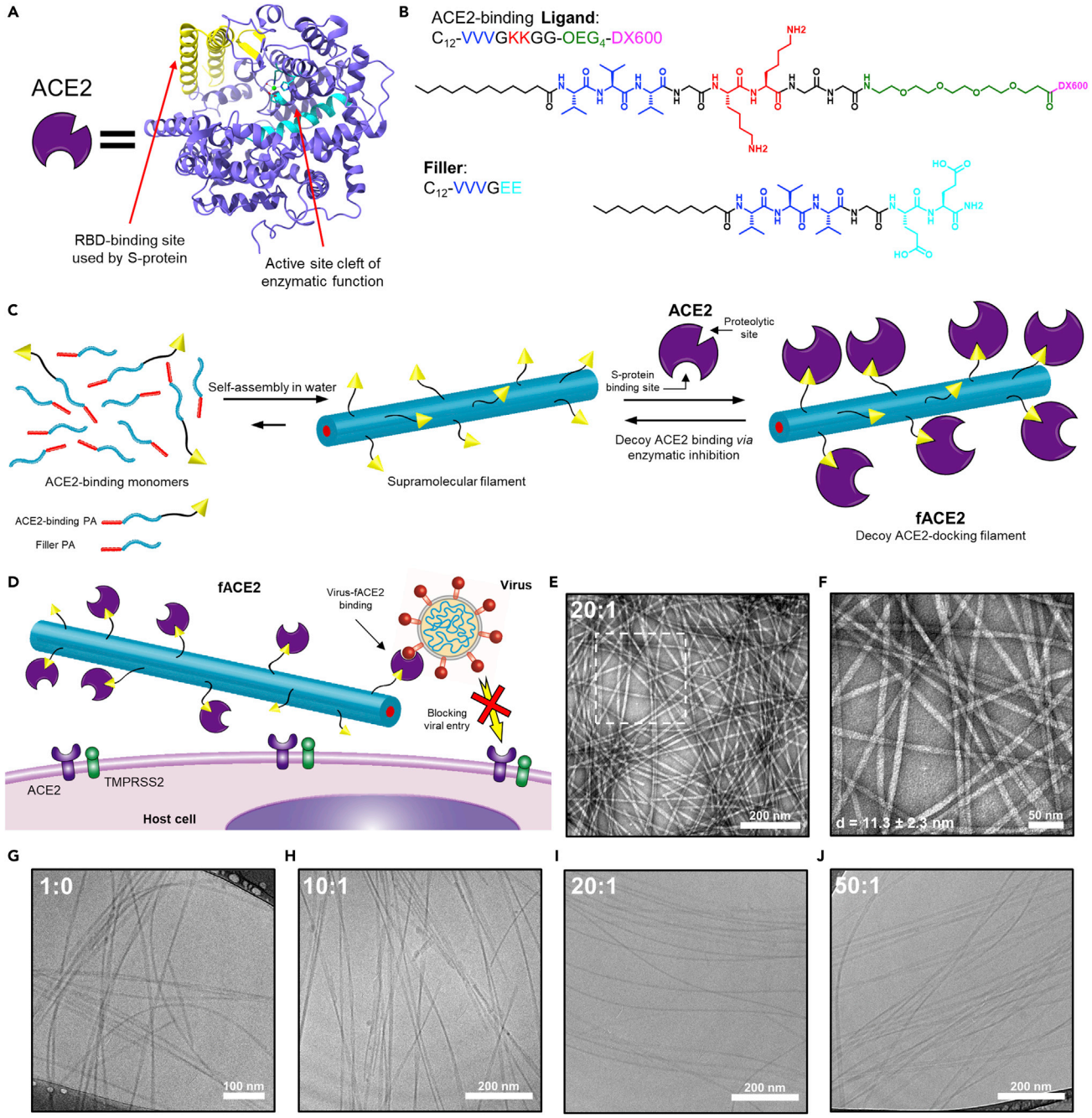

Figure 1. Design of ACE2-docking and silencing supramolecular filaments and their assembly in aqueous solution

(A) Cartoon representation of soluble ACE2 alongside its protein structure, with the SARS-CoV-2 S protein RBD-binding site on ACE2 highlighted in yellow (PDB: 6M17) and the cleft of the carboxypeptidase active site of ACE2 highlighted in cyan (PDB: 1R42). The protein structure was generated using ChimeraX software.

(B) Chemical structure of the investigated ACE2-binding Ligand (top) and Filler (bottom) PA molecules; both contain the same aliphatic region (black) and the same intermolecular hydrogen bond-contributing sequence (blue). The Filler PA contains negatively charged glutamic acid residues (cyan) to pair with the positively charged lysine residues (red) of the Ligand PA. The flexible, hydrophilic spacer (green) of the Ligand PA distances the ACE2-binding peptide DX600 (pink, with amino acid sequence GDYSHCSPLRYYPWWKCTYPDPEGGG) from the surface of assembled supramolecular structures.

(C) The two PAs can be dissolved together in aqueous solution to spontaneously associate and co-assemble into supramolecular filaments that display the ACE2-binding ligand on their surfaces. Subsequently, soluble ACE2 can be added to filament solutions to allow binding via inhibition of the ACE2 proteolytic active site to yield decoy ACE2-docking filaments, called fACE2.

Figure 1. *Continued*
(D) fACE2 can be delivered to nasal passageways and lung tissue, where it can bind to and capture SARS-CoVs to block viral entry into host cells.
(E) Representative low-magnification transmission electron microscopy (TEM) images of ACE2-docking supramolecular filaments (20:1 molar ratio of Filler to Ligand) after dissolving at 1 mM in PBS at pH 7.4 and aging for 24 h, revealing ribbon-like filaments several microns in length. Scale bar represents 200 nm.
(F) High-magnification TEM image of the boxed area in (E). Filament diameter is represented as mean ± SD (n = 35). Scale bar represents 50 nm.
(G–J) Representative cryo-TEM micrographs of ACE2-docking supramolecular filaments formed from co-assembly of varying molar ratios of Filler to Ligand (fixed 50 μM Ligand concentration: G, 1:0; H, 10:1; I, 20:1; and J, 50:1) after dissolving in PBS at pH 7.4 and aging for 24 h, confirming a ribbon-like morphology with slight twisting. Scale bar represents 100 nm (G) or 200 nm (H–J).

the Ligand to optimize ACE2 docking and regulate surface charge.[44] On the C terminus of the Ligand, we present the non-cleavable peptidic ACE2 inhibitor DX600 (K_i = 2.8 nM, K_D = 10.1 nM), through which ACE2 can reversibly bind at its active site,[45] allowing effective immobilization and release of soluble ACE2 from filament surfaces. The DX600 peptide ligand is extended away from the filament surface with a short, flexible, hydrophilic oligoethylene glycol (OEG_4) chain and a double glycine segment (GG) as a spacer for better accessibility and to mitigate undesired interactions between ACE2 and the charged filament surface. The Ligand and Filler were molecularly crafted to have matching but oppositely charged intermolecular interaction-regulating peptide segments (VVVGKK and VVVGEE, respectively) to facilitate formation of a hydrogen bonding network within the filaments (VVV) and to enhance supramolecular cohesion through electrostatic complexation (KK/EE), promoting co-assembly of the two components into filamentous structures.[27,46] Both PAs contain a dodecyl chain (C_{12} alkyl group) at their respective N termini to enable hydrophobic collapse for self-assembly in aqueous environments. Both molecules were synthesized following standard solid-phase peptide synthesis techniques and subsequently purified and characterized with reverse-phase high-performance liquid chromatography (RP-HPLC) and MALDI-TOF mass spectroscopy, respectively (Figures S1 and S2). Together, Ligand and Filler monomers can be mixed at varying ratios in aqueous solutions to spontaneously associate and form supramolecular filaments, and, subsequently, soluble ACE2 can be added to solutions of these filaments to bind to the presented ligand at the surface, yielding ACE2-docking filaments bearing decoy ACE2, called fACE2 (Figure 1C). Solutions of fACE2 can be delivered to nasal passageways and lung tissue, where the presented decoy ACE2 can bind to SARS-CoV spike proteins and block viral entry into host cells, curbing viral infectivity (Figure 1D).

After successful synthesis and purification, the self-assembly behavior of each molecule was studied. After aging for 24 h in water, the Ligand PA alone was observed, using transmission electron microscopy (TEM), to form spherical and other irregularly shaped aggregates, and this shape was corroborated by similar size measurements with dynamic light scattering (DLS) and disordered random-coil circular dichroism (CD) spectra (Figure S3), which is likely due to a combination of a relatively large hydrophilic segment with steric hinderance from neighboring DX600 ligands that hinders the formation of ordered hydrogen bonds between monomers that typically yield one-dimensional structures.[27] Using TEM, the Filler PA was observed to form ribbon-like filaments over several microns in length (Figure S4); thus, the Filler likely not only serves a purpose as a diluting agent to regulate ligand density but is also key for providing dimensionality to the co-assembly of the supramolecular structure components. When mixed together in PBS at pH 7.4, the Ligand and Filler PAs co-assemble into ribbon-like filaments over several microns in length, with diameters measuring around ~11.3 nm under TEM (Figures 1E, 1F, and S4), which is corroborated by the observed increasing β-sheet character of the hydrogen bonding within the filaments as Ligand content is increased (Figure S5).

The ratio of Filler to Ligand PAs in the co-assembled structures is expected to be a key parameter in maximizing ACE2 binding because it determines DX600 density on the filament surface[44] and affects the supramolecular stability of the structures, which is critical for maintaining structural integrity during aerosol formation for inhalable delivery.[36] Because the assembled state represents a dynamic equilibrium between the filaments and monomers, the thermodynamic stability of each PA and their mixture was evaluated by assessing the critical micelle concentration (CMC) for each system via Nile Red assay, revealing CMC values of around 2.9, 1.3, and 0.63 μM for the Filler and Ligand and a 1:1 molar ratio mixture, respectively (Figure S6). By preparing filaments well above the CMC of the Ligand, we can ensure that the majority of the Ligand monomers are incorporated in the supramolecular structure and increase the likelihood of ACE2 docking to the filament surface. The reduction in CMC for the mixed system corroborates the enhanced stability conferred by the additional electrostatic interactions incorporated through opposite charges in our molecular designs and provides additional evidence of co-assembly of the two PAs into supramolecular structures. We varied the molar ratios of Filler to Ligand (10:1, 20:1, and 50:1, with set 50 μM Ligand to be higher than CMC) and observed the resulting supramolecular structures under cryogenic TEM (cryo-TEM) and conventional TEM (Figures 1G–1J and S4). Our cryo-TEM imaging confirms the ribbon-like morphology, with evidence of slight, intermittent twisting for all tested ratios in PBS, suggesting incorporation of the Ligand into filamentous structures with minimal effect on morphology. Our analysis of structure, hydrogen bonding characteristics, and CMC supports supramolecular copolymerization of Filler and Ligand PAs into filaments.

Docking decoy ACE2 to supramolecular filament surfaces

With confirmation of successful incorporation of Ligand PA into supramolecular filaments, we next aimed to assess whether ACE2 can successfully bind to the Ligand PA and dock to filament surfaces. We assessed the specificity of the binding interaction between Ligand and ACE2. We designed a scrambled analog to Ligand, sLigand, in which the order of the amino acids of DX600 are shuffled, to serve as a negative control. Like the ACE2-specific Ligand, sLigand also forms spherical aggregates in water and PBS (Figure S7). Binding of Ligand and sLigand to immobilized ACE2 was analyzed via biolayer interferometry (BLI). We observed a distinct binding response between ACE2 and Ligand compared with sLigand, which demonstrates specificity of the Ligand and ACE2 binding interaction (Figure 2A). For high concentrations above the CMC value, we observe a higher background signal, indicative of nonspecific interactions occurring between the spherical aggregates and ACE2 (Figures 2B and 2C). Because of these solubility limitations of Ligand and sLigand, a binding saturation point was not reached, and an accurate binding affinity constant could not be determined (for the free DX600 peptide, the binding affinity has been reported as K_D = 10.1 nM, where our Ligand likely performs at or below this level).[45] Although we do observe a relatively fast off-rate of ACE2 from Ligand, this rate is likely unimportant in the context of inhibiting viral entry because bound and unbound ACE2 can capture SARS CoVs. Nevertheless, these results support the hypothesis that a specific interaction between Ligand and ACE2 does occur.

We next aimed to verify that the observed binding interaction was occurring at the proteolytic active site of ACE2 and at the surface of the supramolecular structures. Using a fluorogenic peptide substrate for ACE2 (7-methoxycoumarin-4-yl)acetyl-YVADAPK(2,4-dinitrophenyl)-OH (Mca-YVADAPK(Dnp)-OH) where active ACE2 will cleave the quencher moiety from the peptide and yield a detectable

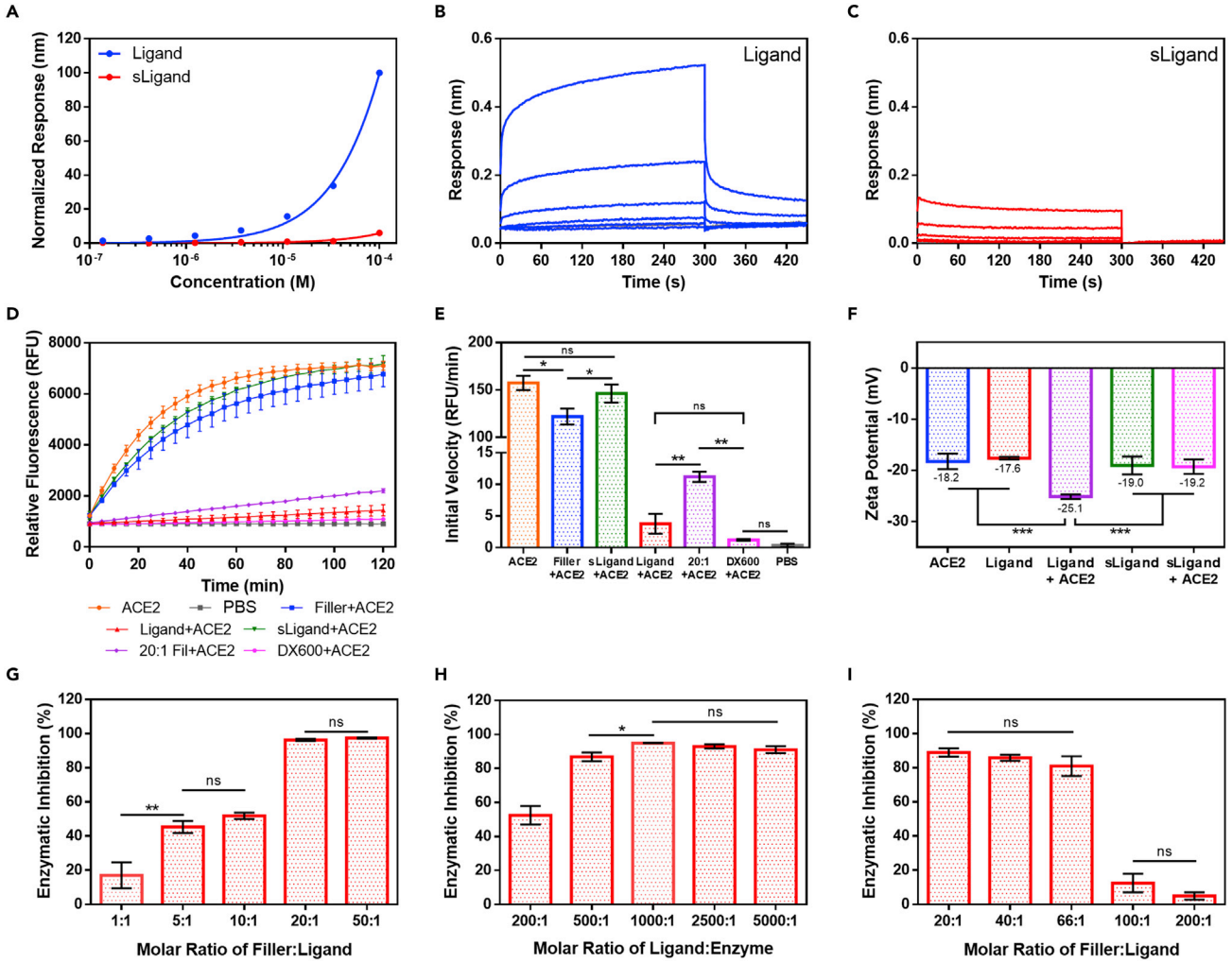

Figure 2. Docking ACE2 to supramolecular filament surfaces via enzyme-substrate complexation

Shown is BLI-based analysis of the interaction kinetics of Ligand and sLigand with immobilized ACE2 by 3-fold dilution (33.3–0.137 μM).

(A) Equilibrium response signal of Ligand and sLigand evaluated a moment before the dissociation step (299 s). Response signals are normalized to their respective maximum values.

(B and C) BLI kinetics traces of (B) Ligand and (C) sLigand association with immobilized ACE2, with the dissociation step occurring at 300 s.

(D) Kinetics measurement of evolved fluorescence of the activity probe by ACE2 cleavage in the presence of various ACE2-docking filament components (ACE2, free rhACE2; 20:1 Fil, 20:1 molar ratio of Filler to Ligand). Data are presented as mean ± SD (n = 3).

(E) Initial velocity calculated from kinetics measurements of ACE2 activity in the presence of ACE2-docking filament components. Data are presented as mean ± SD (*$p < 0.05$; **$p < 0.01$; ns, $p > 0.05$; ****$p < 0.0001$ for ACE2, Filler, and sLigand versus every other group; one-way ANOVA with Tukey's post hoc test, n = 3).

(F) Zeta potential measurements of Ligand and sLigand before and after incubation with ACE2. Data are presented as mean ± SD (***$p < 0.001$; ns, $p > 0.05$ otherwise; one-way ANOVA with Tukey's post hoc test, n = 3).

(G) Effect of Filler:Ligand molar ratio on docking efficiency, holding Ligand (50 μM) and ACE2 (50 nM) concentrations fixed while varying Filler concentration, highlighting optimization of spacing between Ligand PAs within filaments. Data are presented as mean ± SD (**$p < 0.01$; ns $p > 0.05$; ****$p < 0.0001$ otherwise; one-way ANOVA with Tukey's post hoc test, n = 3).

(H) Effect of Ligand:ACE2 molar ratio on docking efficiency, holding Ligand concentration (50 μM) and Filler:Ligand molar ratio (20:1) fixed while varying Ligand:enzyme ratio by adjusting ACE2 concentration. Data represent mean ± SD (*$p < 0.05$; ns, $p > 0.05$; ****$p < 0.0001$ otherwise; one-way ANOVA with Tukey's post hoc test, n = 3).

(I) Effect of Ligand concentration on docking efficiency, holding Filler concentration (1 mM) and Ligand:ACE2 molar ratio (1,000:1) fixed while varying Ligand concentration, reflecting optimization of minimal Ligand concentration to ensure that ACE2 binding occurs with filaments. Data are presented as mean ± SD (ns, $p > 0.05$; ****$p < 0.0001$ otherwise; one-way ANOVA with Tukey's post hoc test, n = 3). Shown is Optimization of co-assembly and loading parameters to maximize ACE2 docking to supramolecular filaments, determined by the extent of enzymatic inhibition relative to free ACE2 control (G–I).

fluorescence signal, we assessed the effect of various components of the ACE2-docking filaments on ACE2 activity (evolved fluorescence for different conditions is shown in Figure 2D). Assuming Michaelis-Menten enzyme kinetics, we also approximated the initial velocity of the reaction (50 nM ACE2) for each condition based on the observed signal (Figure 2E).[45] We observed a slight effect on ACE2 activity in the presence of Filler PA alone, where the small reduction in velocity may likely be attributed to nonspecific interactions between ACE2 and the filaments and also to diffusion limitations presented by a dense filament network (1 mM Filler); however, this activity is much higher compared with the Ligand alone (50 μM), highlighting that DX600 peptide design is key for the ACE2 interaction/inhibition. Compared with the sLigand (50 μM), the Ligand drastically reduces ACE2 initial velocity, confirming that the ACE2-Ligand interaction is occurring at the ACE2 proteolytic site. Although slightly higher, there is no appreciable difference in the initial velocity of ACE2 cleavage in the presence of the Ligand in comparison with the free DX600 peptide alone. For the co-assembled system (20:1 molar ratio of Filler to Ligand), we observed a higher initial velocity compared with the Ligand alone despite equal Ligand concentrations. This could likely be due to a more confined orientation of the DX600 peptide presented on the filament surface, limiting accessibility to ACE2 to some extent, in combination with slower diffusion of ACE2 through the filament network. This reduction relative to the initial velocity of free ACE2 shows around 93% inhibition of added ACE2, suggesting binding to presented inhibitor ligands on the docking filaments.

Next, we aimed to validate that the binding interaction with ACE2 occurs at the surface of the supramolecular structures and not predominately and/or exclusively with monomers in solution. We first conducted zeta potential measurements of ACE2 alone (pI ≈ 5.36) and in the presence of Ligand and sLigand spherical aggregates at physiological pH (7.4) in PBS (Figure 2F) because, if the two entities are not interacting, then we expect the measured zeta potential to be equivalent to the intensity-averaged zeta potential of the mixture. We measured a large drop in zeta potential for the Ligand micelles mixed with ACE2 and relatively no change with the sLigand system, suggesting ACE2 complexation at the particle surface and emphasizing the key role of Ligand binding in facilitating this interaction as opposed to other nonspecific interactions. The lower zeta potential is expected with ACE2 binding because the exposed spike RBD-binding site on ACE2 has a negative electrostatic potential.[47] The same phenomenon is also observed with the co-assembled supramolecular system, where the zeta potential decreases after ACE2 binding, suggesting ACE2 docking at the filament surface (Figure S8).

Optimizing ACE2 presentation on the supramolecular filament surface

To maximize the docking efficiency of added ACE2 and optimize presentation of ACE2 on the surface of the ACE2-docking supramolecular filaments, we investigated the effects of different co-assembly variables in facilitating ACE2 docking, such as molar ratios of the two filament components and relative ACE2 content. First we examined the influence of the Filler:Ligand molar ratio on ACE2 docking efficiency, which we represent as the extent of observed inhibition of ACE2 enzymatic activity for each tested group (initial velocity using a fluorogenic peptide substrate assay) in comparison with free ACE2 activity under the same conditions. For fixed concentrations of Ligand and ACE2 (50 μM and 50 nM, respectively), we observe that, with increasing Filler content relative to Ligand, we achieve greater ACE2 docking (Figures 2G and S9). This is likely reflective of enlarged spacing between neighboring ligands, which facilitates effective ACE2 binding by mitigating steric hinderance that may result from crowding of ligands and/or ACE2 (~85 kDa). With at

least a 20:1 molar ratio of Filler:Ligand, we achieve around 96% of the added ACE2 bound at the filament surface, and higher ratios from this point achieve minimal increases in ACE2 incorporation. We therefore selected the 20:1 ratio as the optimal spacing because this also minimizes Filler demand, which, in turn, decreases the total number of filaments and likelihood of physical crosslinks that can increase solution viscosity and potentially impede ACE2 diffusion, which could have negative effects on the occurrence of binding events between ACE2 and Ligand at filament surfaces.[32,48]

Considering the binding equilibrium that exists between our Ligand, ACE2, and the Ligand-ACE2 complex, we next investigated the effects of the molar Ligand:enzyme ratio, a key parameter in enhancing docking efficiency. Holding the Filler:Ligand ratio (20:1) and Ligand concentration (50 μM) constant, we varied the Ligand:enzyme ratio by adjusting the added ACE2 concentration (10–250 nM) and determined its effect on ACE2 activity inhibition. As expected, we find that, with increasing the Ligand:enzyme ratio, the docking efficiency increases (greater observed enzymatic inhibition) as binding equilibrium is shifted toward formation of the Ligand-ACE2 complex (Figures 2H and S10). With a 1,000:1 molar ratio of Ligand:ACE2 at our optimal ligand spacing, we successfully dock around 95% of the added ACE2 to the filament surface, where further increases show negligible changes in docking efficiency. At higher ACE2 concentrations, docking may be limited by the accessibility of ligands at the filament surface or other steric effects. We selected the 1,000:1 molar ratio of Ligand:ACE2 as optimal for future preparations of fACE2 because this ratio ensures that almost all added ACE2 will bind to the filament surface.

After examining the role of Filler concentration and the ratio of Ligand to ACE2, we next studied the effect of Ligand concentration on maximizing docking efficiency. Although holding the Filler concentration constant (1 mM) and varying added ACE2 to maintain a 1,000:1 molar ratio of Ligand:ACE2, we adjusted the Ligand content in the filaments (5–50 μM) and determined its effect on ACE2 activity (Figures 2I and S11). We observe that increasing the ligand concentration yields greater docking of ACE2, as expected. We also see a drastic drop in ACE2 docking with the lower concentrations of Ligand tested (10 μM), suggesting the existence of a critical point in Ligand concentration where, despite being at the optimal ratio relative to ACE2, the density of Ligand is too low, and the equilibrium is likely not shifted in favor of formation of the Ligand-ACE2 complex. At these lower concentrations of Ligand, the probability of ACE2 binding to a presented Ligand molecule is too low (whereas, for the study detailed in Figure 2G, the Ligand concentration held at a constant reflects an equal probability of a binding event between conditions). These results validate that, without presentation of the enzymatic inhibitory ligand at their surface, there is negligible interaction of ACE2 with the filaments. Last, we determined the minimal incubation time sufficient to achieve the maximum docking efficiency of added ACE2. At the previously determined optimal conditions for ACE2 docking (20:1 Filler:Ligand and 1,000:1 Ligand:ACE2), we pre-incubated filaments with ACE2 (25 nM) for a range of times (0–120 min) before assessing ACE2 activity (Figure S12). We observed an almost instantaneous capture of ACE2 to the filament surface (0 min incubation, ~83% inhibition), which is likely due to the strong binding affinity of the DX600 ligand for ACE2. Within 15 min, we achieve the maximum docking efficiency of around 95%, with longer incubation times showing negligible increases in ACE2 inhibition. This is promising with respect to translation of the system to a clinical setting because ACE2 will dock to filament surfaces within a few minutes, yielding fACE2 ready for administration.

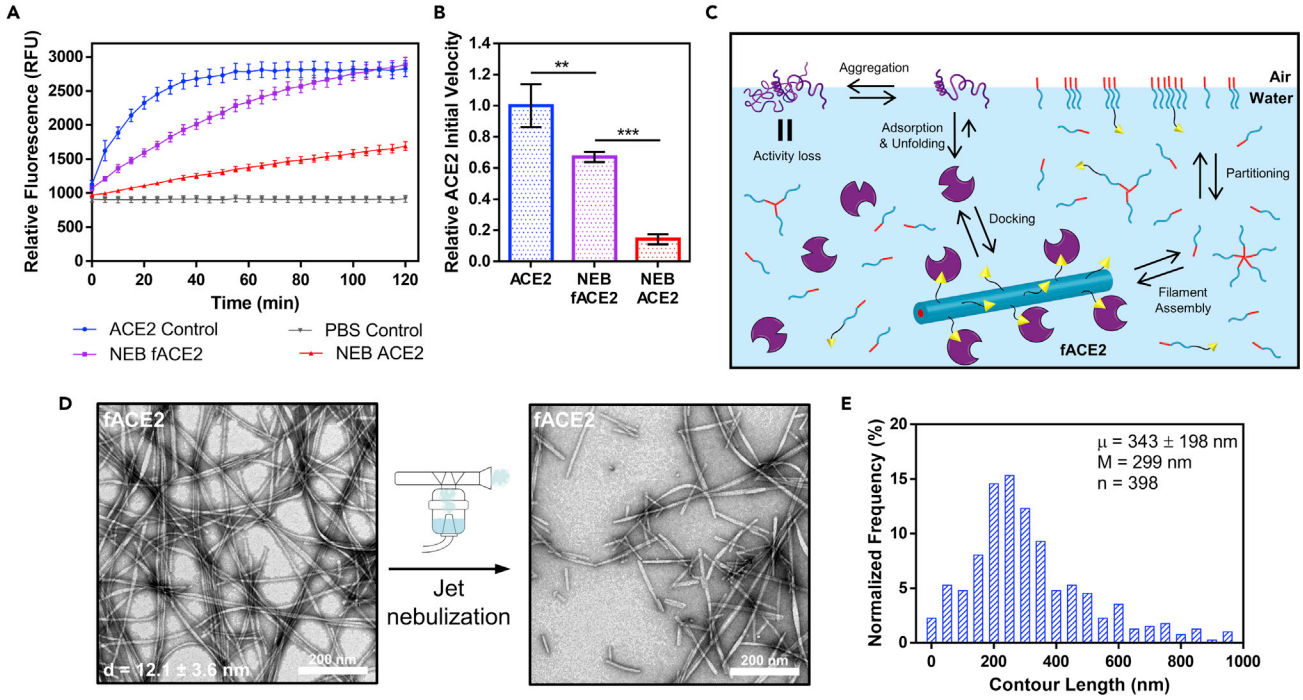

Figure 3. Delivery of fACE2 in respirable aerosols via jet nebulization

(A) Kinetics measurement of evolved fluorescence intensity of the proteolytic activity probe by ACE2 after nebulization and after separation of ACE2 from filaments via dialysis, highlighting the increased ACE2 activity afforded by fACE2 compared with free ACE2. Data represent mean ± SD (n = 3).

(B) Estimated initial velocities of ACE2 proteolytic activity, determined from kinetics measurements (relative to free ACE2 control), emphasizing the preservation effect afforded by the docking strategy. Data are presented as mean ± SD (**p < 0.01, ***p < 0.001, ****p < 0.0001 for ACE2 versus NEB ACE2, one-way ANOVA with Tukey's post hoc test, n = 3).

(C) Schematic of the hypothesized mechanism of ACE2 structural preservation afforded by fACE2, where binding affinity interactions of ACE2 at the filament surface and enrichment of the air-liquid interface (ALI) by filament PA monomers mitigate the interaction strength of ALI on ACE2 together prevent protein unfolding and aggregation, preserving ACE2 activity.

(D) Representative TEM images of fACE2 at 1 mM in PBS at pH 7.4 before (left) and after (right) jet nebulization, showing retention of filament shape but reduction in length. Diameter measurements are represented as mean ± SD (n = 35). Scale bar represents 200 nm.

(E) Population size distribution of observed filament contour lengths after jet nebulization of fACE2 (20 bins, 50 nm each) from TEM images, where average contour length (μ) is given as mean ± SD alongside median (M) length (n = 398 analyzed filaments).

Delivery of fACE2 in respirable aerosols

Having validated successful docking of ACE2 to the supramolecular filament surface, we next evaluated the ability of the filaments to carry ACE2 in respirable aerosols as a means of delivering ACE2 directly to lung tissues via jet nebulization. Because of the noncovalent nature of filament assembly and binding of ACE2, we expect structural integrity and activity to be affected by air-liquid interface (ALI) enrichment and shear stress during aerosol droplet formation.[36,49,50] This is of particular importance with respect to the decoy function of ACE2 because potential ACE2 unfolding and aggregation from aerosolization may negatively influence the ability of the viral S protein to effectively bind to decoy ACE2. We therefore investigated the stability of docked ACE2, reflected by its proteolytic activity (because unfolded and/or aggregated ACE2 will likely exhibit inhibited activity), by collecting and analyzing the emitted mist from a jet nebulizer, after which ACE2 was unbound and separated from filament surfaces by dialysis. Although reduced compared with pre-nebulization, we find that ACE2 delivered on filaments exhibits much higher enzymatic activity (around 67% relative initial velocity relative to the ACE2 control) compared with free ACE2 (around 14% relative to the control) after jet nebulization (Figures 3A and 3B). These results suggest that our docking strategy not only facilitates delivery

of decoy ACE2 in respirable aerosols but also provides protection against protein denaturization by harsh aerosolization forces, ensuring greater fractions of delivered ACE2 in the correct conformation. We speculate that two factors contribute to the structural preservation of ACE2 in this system (shown in Figure 3C). First, the strong binding affinity of ACE2 to the Ligand molecule likely aids in mitigating adsorption of ACE2 to the highly hydrophobic ALI, which can result in protein unfolding and aggregation, by shifting the equilibrium toward the docked state and reducing ACE2 content in the bulk solution. Second, the PA monomers of the supramolecular filaments exchange frequently between their assembled state and the ALI, where the hydrophobic influence of the ALI shifts the assembly-disassembly equilibrium from the supramolecular structure to the monomeric form.[36,51] Subsequent enrichment of the ALI by PA monomers likely impedes ACE2 adsorption and potential unfolding and/or aggregation, preserving its structure and activity. Therefore, using supramolecular filaments as inhalable carriers appears to be highly advantageous for protein delivery within respirable aerosols, particularly because of the surface activity of PAs. Based on this proposed mechanism, improvements to ACE2 activity and structure preservation could be afforded by increasing the strength of the binding interaction between ACE2 and the filament surface (such as using a tighter binder to the proteolytic active site in the Ligand design) and/or optimizing the extent of interface enrichment of the PAs to aerosol droplet surfaces (by modulating their CMCs).

To further elucidate the behavior of fACE2 during aerosol delivery, we next assessed its structural stability during jet nebulization. This is of concern because filaments measure over several microns in length and form from noncovalent interactions, and the resulting size distribution after nebulization will be critical for achieving ideal distribution and retention of fACE2 in lung tissue.[39,52] As observed with TEM, fACE2 maintains its ribbon-like morphology after addition of ACE2 (50 nM), and after jet nebulization, fACE2 maintains its filamentous shape with an observed reduction in contour length, which is expected because of ALI enrichment and shear during aerosol droplet formation (Figure 3D).[36,53] The influence of these factors is corroborated by CD measurements, where the observed reduction in signal intensity is reflective of weakened hydrogen bonding because of dissociation into smaller structures and/or PA monomers (Figure S13). The average contour length of fACE2 after nebulization measured around 343 $\pm$ 196 nm, although nebulization does induce polydispersity with respect to filament length (Figure 3E). However, this distribution of size could be advantageous with respect to diffusion through the mucus layer atop airway epithelia because some fACE2 may penetrate the mucus and some remains on top of or closer to the mucus layer surface.[39] Integration of fACE2 throughout the mucus layer may potentially increase the likelihood of successful virus capture before viral entry into host cells. The degree of filament fragmentation is consistent regardless of formulation concentration (0.2–1 mM filament concentration range), where the average contour length is around 330 nm, with similar distributions for each tested concentration (Figure S14). Jet nebulizer emission of fACE2 is linear over the course of a nebulization event, with release of around 6.3%/min (by mass) of the loaded dose (Figure S15). These data suggest that fACE2 exhibits steady release from a jet nebulizer with consistent size distribution, which is imperative for achieving more uniform distributions in lung tissue for inhalation-based delivery.

Inhibition of pseudotyped CoV entry *in vitro* by fACE2

Having shown that ACE2-docking filaments bind ACE2 to their surface and carry ACE2 in respirable aerosols, we next evaluated the ability of fACE2 to capture SARS-CoV-1 and -2 spike protein pseudotyped feline immunodeficiency virus (FIV)

and prevent viral entry *in vitro*. First we assessed the cytotoxicity of ACE2-docking filaments against relevant human cell lines (NL20, bronchial epithelial cells; A549, alveolar basal epithelial adenocarcinoma cells; and 293/ACE2/TMPRSS2, stable-producing human ACE2 and co-receptor, TMPRSS2,[12] HEK293 cells, used in following antiviral studies). For all tested concentrations of filaments (0.1–100 μM), cells maintained high viability after treatment (>90%), which is promising for use of this system as a safe delivery vehicle of soluble ACE2 (Figure S16). The negligible cytotoxicity likely does not interfere with evaluation of antiviral efficacy in the following *in vitro* assessments.

To evaluate the antiviral effect of fACE2, pseudotyped viruses (PsVs) were generated for SARS-CoV-2 and SARS-CoV (with vesicular stomatitis virus G protein [VSV-G] as a negative control) to yield virus particles decorated with their respective spike protein and containing an expression cassette for luciferase to assess viral entry into 293/ACE2/TMPRSS2 cells. We first assessed the decoy effect of fACE2 and relevant controls (free recombinant human [rhACE2] and empty ACE2-docking filaments [20:1 molar ratio Filler:Ligand filaments without ACE2 docked to their surface, Fil]) by pre-incubating varying doses with each PsV and subsequently challenging 293/ACE2/TMPRSS2 cells with the mixture (Figure 4A). We found that SARS-CoV-2 and SARS-CoV PsV infection is strongly inhibited by fACE2 and ACE2 in a dose-dependent manner, suggesting that ACE2 displayed on the surface of fACE2 hijacks S protein-mediated viral infection and that docking of ACE2 does not impede viral capture (Figures 4B and 4C). This trend is not observed for the VSV-G PsV, as expected, and the empty filaments alone show little to no viral capture for all PsVs tested, emphasizing the key role of ACE2 in inhibiting S protein-mediated viral entry. An increase in inhibition is observed at higher concentrations of filaments (~18% at the highest dose against SARS-CoV-2 PsV), which may be due to nonspecific interactions between virus particles and filaments; this may explain the higher PsV infection inhibition observed for fACE2 (~88%) compared with free ACE2 (~66%). Against SARS-CoV-2 and SARS-CoV, fACE2 exhibited potent inhibitory activity, which shows promise in providing broad-spectrum antiviral efficacy for current and future SARS-CoVs.

Because ACE2 degrades quickly, extending its availability as a decoy is highly desirable for blocking SARS CoV infections.[19] Therefore, we next aimed to assess the preventative effect of fACE2 and whether our docking strategy serves to extend the decoy function. To achieve this, we pre-treated 293/ACE2/TMPRSS2 cells with fACE2 and relevant controls (0.5 nM ACE2 dose) and allowed them to incubate for a set time before challenge with SARS-CoV-2 PsV (Figure 4E). We observed that, for all tested incubation times, fACE2 exhibited a greater inhibitory effect compared with free ACE2; the extent of inhibition by free ACE2 began to steadily decrease around 2 h and became almost identical to empty filaments by 6 h (Figure 4F). In stark contrast, fACE2 inhibitory potential declined at a much slower rate, maintaining around ~60% inhibition of PsV infection at 6 h. The preventative effect was assessed for longer incubation times for fACE2 and empty filaments (excluding ACE2 because the inhibitory effect became equivalent to that of the empty filament control). After 12 h, fACE2 preventative efficacy begins to wane and becomes indistinguishable from that of empty filaments around 36–48 h (Figure 4G). These results highlight a key advantage of fACE2 in preventing viral entry, where it exhibits more potent and sustained inhibitory efficacy compared with free ACE2, likely because of docking to the filament surface. Binding of ACE2 to the filament likely impedes premature degradation and/or cellular uptake of ACE2, enhancing and prolonging its antiviral efficacy.

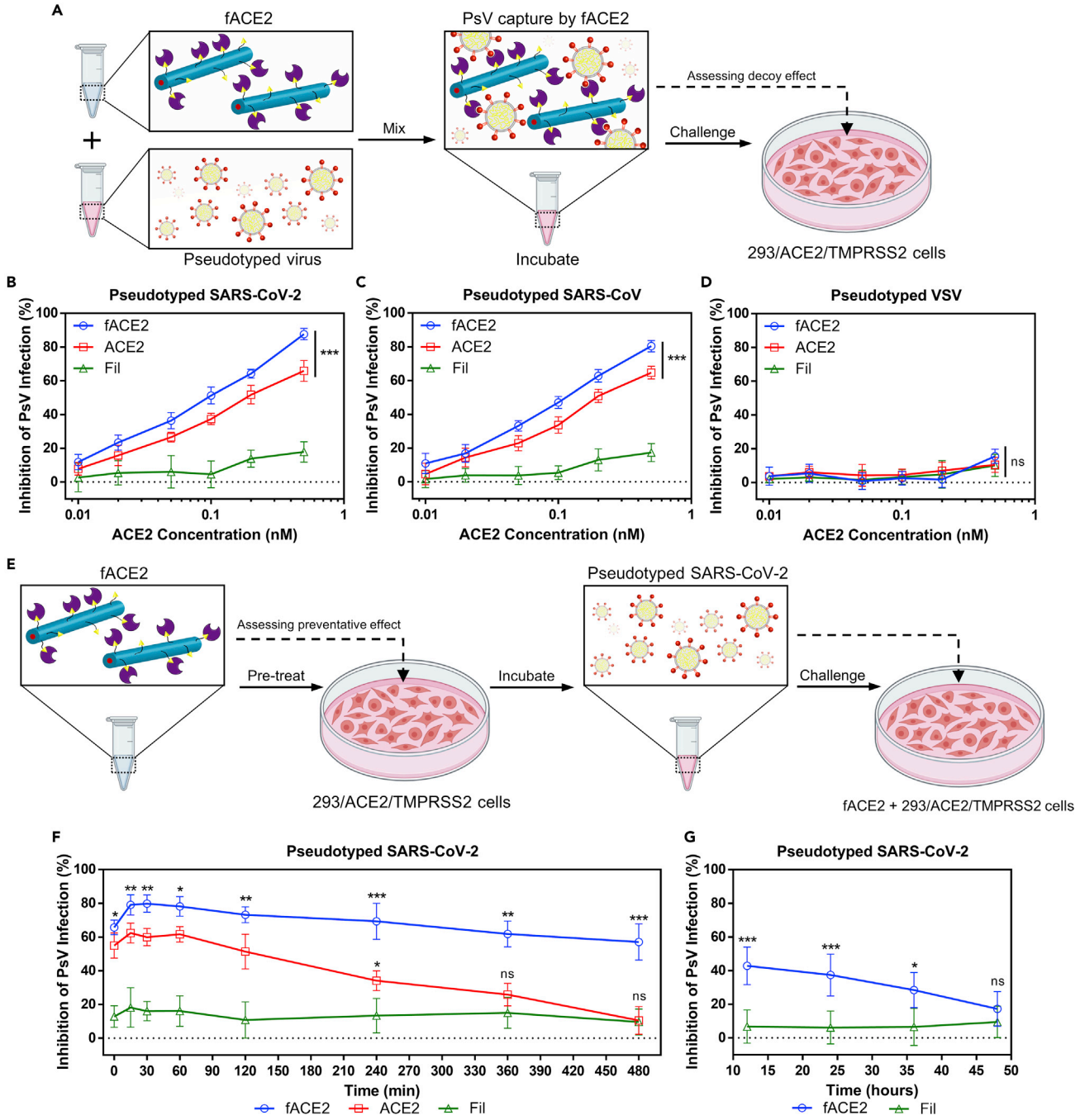

Figure 4. fACE2 inhibits PsV infection and docking of ACE2 extends its decoy function

(A) Schematic of the study design for assessing the decoy effect of fACE2.

(B–D) Shown is inhibitory activity of fACE2 and controls (rhACE2 and empty filaments [20:1 molar ratio Filler:Ligand filaments without ACE2 docked to their surface]; Fil) against PsV. SARS-CoV-2 (B), SARS-CoV (C), and VSV (D) viral entry. Data are presented as mean ± SD (for the highest tested dose: ns, $p > 0.05$; ***$p < 0.001$; ****$p < 0.0001$ for fACE2 and ACE2 versus Fil for SARS-CoV-2 and SARS-CoV PsV; one-way ANOVA with Tukey's post-hoc test, n = 3 independent experiments).

(E) Schematic of the study design for assessing the preventative effect of fACE2 against SARS-CoV-2 PsV challenge.

(F) Inhibitory activity of fACE2 and controls after set incubation times against SARS-CoV-2 PsV viral entry evaluated at 0.5 nM ACE2 or the equivalent dose. Data are presented as mean ± SD (ns, $p > 0.05$; *$p < 0.05$; **$p < 0.01$; ***$p < 0.001$, with fACE2 versus ACE2 represented above the fACE2 line and ACE2 versus Fil above the ACE2 line; ****$p < 0.0001$ for fACE2 and ACE2 versus Fil otherwise; one-way ANOVA with Tukey's post hoc test, n = 3 independent experiments).

(G) Inhibitory activity of fACE2 and Fil after set incubation times (continuing from F) against SARS-CoV-2 PsV viral entry. Data are presented as mean ± SD (for each time point: ns, $p > 0.05$; *$p < 0.05$; ***$p < 0.001$, unpaired two-tailed t test with Welch's correction, n = 3 independent experiments).

Attenuation of SARS-CoV-2 viral loads *in vivo* by inhalation of fACE2

After demonstrating the enhanced and extended antiviral efficacy afforded by our docking strategy against pseudotyped FIV, we next assessed the efficiency of fACE2 delivery into the lungs and its ability to subsequently capture SARS-CoV-2 *in vivo*. For delivery to mice, we used an intranasal mucosal atomizer to subject fACE2 to shear forces necessary to generate respirable aerosols before administration, which also yielded filaments of reduced contour length (Figure S17). By loading ACE2-docking filaments with a near-infrared fluorescent dye (Cyanine 5.5) to allow *in vivo* visualization, we evaluated the distribution and retention of the ACE2-docking filaments administered via intranasal inhalation and intratracheal instillation into K18-hACE2 transgenic mice. 3 h after administration, the fluorescence signal is still detectable in nasal passageways of treated mice, evidencing the presence of filaments. After 24 h, excised lungs show a strong fluorescence signal throughout the distal lungs, suggesting migration and long-term retention of filaments, which may likely be afforded by their filamentous shape (Figure S18).[54,55] Histology of lung tissue sections taken at the 24-h time point indicates no obvious signs of structural damage, apoptosis, inflammation, or neutrophil infiltration induced by treatment with ACE2-docking filaments compared with the PBS control (Figure S19). These results suggest that ACE2-docking filaments exhibit long-term retention within lung tissues after inhalation and are safe, biocompatible delivery vehicles for ACE2.

Having achieved successful inhalation delivery of ACE2-docking filaments *in vivo*, we next assessed the clinical potential of fACE2 as a preventative therapeutic agent against CoV infection. As shown in Figure 5A, we administered atomized fACE2 (20 nM dose of ACE2), rhACE2 (20 nM), or empty filaments (equivalent to the 20 nM ACE2 dose) to K18-hACE2 mice via intranasal inhalation 1 h before inoculating mice with prototype SARS-CoV-2 virus (USA-WA1/2020, 10^5 plaque-forming units [PFUs]/mouse). 2 days after inoculation, the mice were euthanized, and their lung tissue was harvested. As evidenced by increased cycle threshold (Ct) values for N protein gene expression and reduced N protein detection in lung tissue, treatment with fACE2 greatly reduces viral load in SARS-CoV-2-infected lungs compared with empty filaments and rhACE2 alone (Figures 5B and 5H), although the body weight loss in each group was similar (Figure 5C). The similar negligible effect on viral load by empty filaments and free rhACE2 suggests that the observed enhanced efficacy of fACE2 can likely be attributed to structural and functional preservation of ACE2 by our docking strategy as opposed to nonspecific interactions between filaments and virus particles. In parallel with the reduced viral load, mice that received treatment with fACE2 also exhibited decreased expression of the pro-inflammatory cytokine interleukin-6 (IL-6; Figure 5D), a hallmark of the hyperinflammatory response and cytokine storm in human and animal models of SARS-CoV-2 infection.[56–58] Enhanced expression of the antiviral cytokine interferon gamma (IFN-γ; Figure 5E) was observed, suggesting restored antiviral immune responses and balanced inflammatory responses, which are typically lacking in patients with progressing COVID-19 and animal models and are indicative of severe COVID-19.[59–62] fACE2-treated mice displayed alleviated lung inflammation and related pathology, as evidenced by mitigated inflammatory cell infiltration into lung tissue (neutrophils and monocytes; Figures 5F, 5G, and S20).[63] These results highlight the prophylactic and therapeutic potential afforded by our docking strategy of decoy ACE2 to filament surfaces to improve antiviral efficacy, clearly illustrating the preventative potential of fACE2 in clinical practice. Although preventative efficacy is directly investigated here, these results also highlight the potential of fACE2 as a treatment tool for those already infected with SARS-CoV-2 by reducing

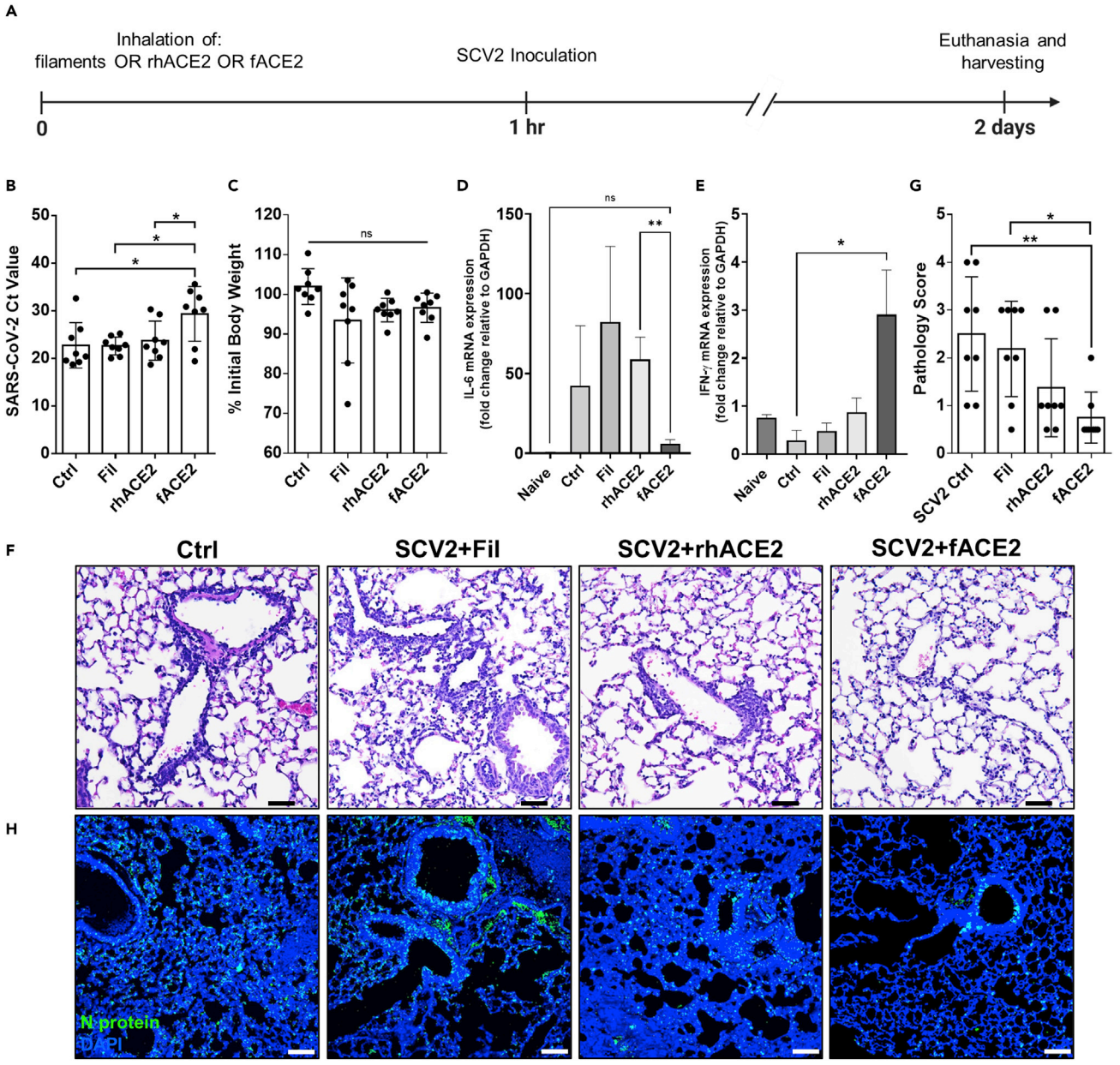

Figure 5. fACE2 attenuates viral load and lung injury after SARS-CoV-2 inoculation *in vivo*

(A) Experimental timeline to assess the effectiveness of fACE2 and controls delivered via inhalation in mitigating the viral infectivity of subsequent SARS-CoV-2 inoculation (USA-WA1/2020, 1.5 × 10^5 $TCID_{50}$ dose) in K18-hACE2 transgenic mice.

(B) Ct values of SARS-CoV-2 in harvested lungs of K18-hACE2 mice after treatment with atomized fACE2 (20 nM ACE2 dose in PBS) and controls (Ctrls, PBS; Fil, atomized equivalent empty filament dose in PBS (20:1 molar ratio Filler:Ligand filaments without ACE2 docked to their surface); rhACE2, recombinant human ACE2, 20 nM dose in PBS). Data are presented as mean ± SD (*$p < 0.05$; ns, $p > 0.05$ otherwise; one-way ANOVA with Tukey's post hoc test, n = 8 mice per group).

(C) Change in mouse body weight as a percentage of initial weight 2 days after treatment and SARS-CoV-2 inoculation. Data are presented as mean ± SD (ns, $p > 0.05$, one-way ANOVA with Tukey's post-hoc test, n = 8).

(D) Pro-inflammatory cytokine interleukin-6 (IL-6) mRNA expression from harvested mouse lungs by qRT-PCR after treatment and SARS-CoV-2 inoculation (the "naive" group represents expression levels in healthy, untreated, and unchallenged mice). Data are presented as mean ± SD (**$p < 0.01$; ns, $p > 0.05$ otherwise; one-way ANOVA with Tukey's post hoc test, n = 8).

(E) Antiviral cytokine interferon gamma (IFN-γ) mRNA expression from harvested mouse lungs by qRT-PCR after treatment and SARS-CoV-2 inoculation (the "naive" group represents expression levels in healthy, untreated, and unchallenged mice). Data are presented as mean ± SD (*$p < 0.05$; ns, $p > 0.05$ otherwise; one-way ANOVA with Tukey's post hoc test, n = 8).

Figure 5. *Continued*

(F) Hematoxylin and eosin (H&E) staining of harvested mouse lung tissue sections after treatment and SARS-CoV-2 inoculation. Scale bars represent 50 μm.

(G) Summary of pathology scoring of analyzed mouse lung tissue sections as described in the Supplemental experimental procedures. Data are presented as mean ± SD (*$p < 0.05$; **$p < 0.01$; ns, $p > 0.05$ otherwise; one-way ANOVA with Tukey's post hoc test, n = 8).

(H) IF staining of harvested mouse lung tissue sections after treatment and SARS-CoV-2 inoculation, showing SARS-CoV-2 N protein (anti-SCV2 N protein antibody, green) and nucleus (DAPI, blue) signals. Scale bars represent 50 μm.

the viral load in the airways and distal lungs through trapping newly replicated and released viral particles at the sites of infection.

Conclusions

In this work, we demonstrate the development of peptide-based supramolecular filaments for delivery of ACE2 in inhalable aerosols to capture SARS-CoVs and prevent infection for a prolonged period of time. Through incorporation of a peptide that inhibits the carboxypeptidase activity of ACE2 into our design, we are able to dock ACE2 to the surface of supramolecular filaments through enzyme-substrate complexation while leaving the spike protein RBD-binding site exposed. This docking strategy enables us to silence ACE2's enzymatic activity, while stabilizing ACE2 for nebulization and inhalable delivery and increasing its retention in lung tissue when inhaled as a respirable aerosol. We demonstrate that fACE2 can act as a decoy for viral binding, as evidenced by enhanced and prolonged reduction of SARS-CoV-2 viral load *in vitro* and *in vivo*, and this reduction in viral load is able to prevent lung damage. Future work will investigate the therapeutic potential of fACE2 for treating COVID-19. This study establishes that our novel fACE2 system has high translational potential to prevent current and future CoV infections, affording a new platform for inhalable delivery of protein therapeutic agents to treat other human diseases.

EXPERIMENTAL PROCEDURES

Resource availability

Lead contact

Further information and requests for resources and reagents should be directed to and will be fulfilled by the lead contact, H.C. (hcui@jhu.edu).

Materials availability

The materials generated in this study are available from the lead contact upon request. This study did not generate new unique reagents.

Data and code availability

The data used to support the findings of this study are available from the lead contact upon request. This paper does not report original code.

Materials and reagents

All fluorenylmethyloxycarbonyl (Fmoc)-protected amino acids and resins were purchased from Advanced Automated Peptide Protein Technologies (Louisville, KY). The OEG4 spacer (Fmoc-N-amido-PEG4-acid) was purchased from BroadPharm (San Diego, CA). rhACE2 protein (carrier free) was purchased from R&D Systems, Bio-Techne (Minneapolis, MN). Biotinylated human recombinant (His tag) ACE2 protein was purchased from Sino Biological (Wayne, PA). Free DX600 peptide used as a control was purchased from Cayman Chemical (Ann Arbor, MI). The near-infrared fluorescent dye Cyanine 5.5 carboxylic acid was purchased from Lumiprobe (Hunt Valley, MD). All other reagents and solvents were sourced from VWR, Avantor (Radnor, PA) or Sigma-Aldrich, Millipore Sigma (St. Louis, MO) without any further purification unless otherwise indicated.

Molecular self-assembly and co-assembly of PAs to form supramolecular structures

For self-assembly of PAs, lyophilized powders of PA were dissolved in 200 μL of hexafluoro-2-propanol (HFIP) to disrupt any preassembled structures. Samples were vortexed and sonicated for 5 min to aid dissolution and mixing. For co-assembled systems, appropriate volumes of Ligand solutions were added to solutions of Filler to achieve the specific molar ratios used in this study (Filler:Ligand ranging from 1:1–200:1 molar ratio), and tubes of the mixtures were vortexed and sonicated for 5 min to aid dissolution and mixing of the 2 components. Next, HFIP was evaporated and dried under a vacuum overnight to remove all traces of HFIP. After drying, Milli-Q water or PBS was added to yield the appropriate final concentrations (1 mM for Filler alone and 1 mM Filler for all co-assembly systems; 200 μM Ligand and sLigand alone and varied concentrations of Ligand relative to Filler for all co-assembly systems) of PAs and then vortexed to aid dissolution. The pH of the solutions was then adjusted with addition of 0.1 M HCl(aq) and 0.1 M NaOH(aq) to yield a final pH of 7.4. The solutions were then heated at 80°C in a water bath for 1 h to aid dissolution and facilitate the annealing process and then cooled at room temperature overnight. For docking of ACE2 to filament surfaces, solutions of ACE2 in PBS were mixed with filament solutions at an equal volume and allowed to incubate at room temperature for a set time until use, yielding fACE2.

For encapsulation of the near-infrared dye Cy5.5 (Cyanine 5.5 carboxylic acid, Lumiprobe, Hunt Valley, MD) into hydrophobic filament cores, the same procedure was followed as described above; Cy5.5 was dissolved with filament components in HFIP at 2:1 molar excess relative to the Filler. After removal of HFIP, dissolution in PBS, annealing, and aging overnight, unencapsulated Cy5.5 (precipitated) was removed by centrifugation (13,400 rpm, 3 min), and filament-containing supernatant was removed for analysis and *in vivo* lung distribution studies.

TEM and cryo-TEM

Solutions of PAs were added (10-μL drop) onto a carbon film copper grid (400-square mesh, Electron Microscopy Sciences, Hatfield, PA) and allowed to sit for 1 min. Then the excess solution was wicked away with filter paper to leave a thin film of the sample on top of the grid. To achieve negative staining, a 7-μL droplet of uranyl acetate solution (2 wt % in Milli-Q water) was added on top of the grid and blotted away after 30 s. Grids were left to dry for at least 3 h before imaging on an FEI Tecnai 12 Twin transmission electron microscope (100-kV acceleration voltage). All images were recorded using an SIS Megaview III wide-angle charge-coupled device (CCD) camera. Filament diameters and contour lengths were measured using ImageJ software (NIH, Bethesda, MD); a minimum of 35 individual structures were analyzed for diameter length measurements, and a minimum of 350 separate filamentous structures were analyzed for contour length measurements.

For cryo-TEM, lacey carbon-coated copper grids (Electron Microscopy Sciences, Hatfield, PA) were treated with plasma air for 30 s before sample preparation to render the lacey carbon film hydrophilic. Sample addition to the grids was achieved with a Vitrobot with a controlled humidity chamber (FEI, Hillsboro, OR) maintained at 95% humidity. Droplets of sample solutions (in PBS at pH 7.4, 6 μL) were added to suspended grids in the Vitrobot and allowed to sit for 1 min before the grid was blotted with filter paper using Vitrobot preset parameters and then immediately plunged into a liquid ethane reservoir precooled by liquid nitrogen to produce a thick vitreous ice film on the surface of the grid. The grids were then transferred to

a cryo-holder and cryo-transfer stage that were also cooled by liquid nitrogen. All imaging was performed on an FEI Tecnai 12 Twin transmission electron microscope, operating at a 100-kV acceleration voltage. The cryo-holder temperature was maintained below −170°C with liquid nitrogen to prevent sublimation of vitreous water during imaging. All images were acquired with a 16-bit 2K × 2K FEI Eagle bottom-mount camera.

ACE2 activity assays

The fluorogenic peptide substrate Mca-YVADAPK(Dnp)-OH (R&D Systems, Bio-Techne, Minneapolis, MN), was diluted from stock (4 mM) to a final concentration of 1 mM in dimethyl sulfoxide (DMSO). All monitored reactions with ACE2 were conducted in black, 96-well, flat-bottom, tissue culture-treated microplates (Falcon, Corning, NY) in 100 μL of PBS (pH 7.4) at room temperature with substrate (1–5 μL, 10–50 μM final concentration, DMSO concentration maintained at ≤5% [v/v]) added immediately before measurement. An equal volume of ACE2 was added to solutions of the supramolecular structure and incubated for 1 h for all experiments unless stated otherwise. ACE2 activity was monitored continuously (every 5 min for 2 h total) by measuring fluorescence intensity (λ_{ex} = 320 nm, λ_{em} = 405 nm) upon substrate hydrolysis using a SpectraMax M3 microplate reader (Molecular Devices, San Jose, CA). The initial velocity for each reaction was determined from the rate of fluorescence evolved over the 5- to 20-min time course (the slope from linear regression analysis of this region). The extent of enzymatic inhibition (used as a reflection of the docking efficiency of ACE2 to the filament surface) was determined as the measured initial velocity of a tested condition relative to free ACE2 at the same ACE2 and substrate concentration.

Aerosolization of ACE2-docking filaments and fACE2

For studies involving jet nebulization of ACE2-docking filaments and fACE2, solutions of these (3 mL) were added to a disposable jet nebulizer (Neb Kit 500, Drive Medical, Port Washington, NY) and connected to a nebulizer compressor (Rite-Neb 4, ProBasics, Marlboro, NJ) for constant air flow supply (~6–10 L/min). The emitted mist was collected by fitting the outlet of the nebulizer with a 50-mL conical tube, where liquid aerosol droplets condense on the walls of the tube. Then the conical tubes were centrifuged at 4,000 rpm for 3 min, and the collected solution was removed for analysis.

For quantification of ACE2 activity after nebulization, emitted mist solutions of fACE2 were dialyzed against PBS for 48 h using a Spectra/Por Float-A-Lyzer G2 dialysis device (MWCO, 20 kDa; Spectrum Labs, Rancho Dominquez, CA) to facilitate ACE2 separation from filaments before analysis.

For the release rate of ACE2-docking filaments from the nebulizer, the device was weighed before and after addition of filament solutions (3 mL). For the course of a 10-min nebulization event, solution in the reservoir (50 μL) was collected at 2-min intervals, and the nebulizer with the remaining solution was weighed, and mass was recorded. Using analytical HPLC, the collected reservoir samples were assessed to determine the concentration of filaments left over at each time point. Using gravimetric data and the analyzed concentrations, release profiles were determined for the filaments via mass balance analysis.

For *in vivo* studies involving inhalation delivery of ACE2-docking filaments to mice, filament solutions were loaded into a BD Luer-Lok 1-mL syringe equipped with a, MAD Nasal intranasal mucosal atomization device (Teleflex Medical, Morrisville, NC) to emit

liquid droplets by pushing solution through the syringe. Collected solutions were used for administration to mice (inhalation or intratracheal instillation).

Inhibition of pseudotyped virus (PsV) infection *in vitro*

SARS-CoV and SARS-CoV-2 S protein cDNA (a gift from Dr. Marc Johnson, University of Missouri School of Medicine) was used to pseudotype FIV expressing luciferase using methods described previously.[64] A VSV-G protein pseudotyped FIV expressing luciferase was used as a positive control for viral transduction.

For the dose-response decoy effect studies (Figures 4A–4D), prior to infection, 2 μL of PsV (PsV titers: SARS-CoV-2, 1.7×10^{14} virus particles [VP]/mL; SARS-CoV, 1.7×10^{14} VP/mL; VSV, 4.0×10^{14} VP/mL) was added to 100 μL of Opti-MEM medium (Gibco, Invitrogen) supplemented with 2% (v/v) fetal bovine serum (FBS); 10 μL of fACE2, free ACE2, or empty ACE2-docking filaments (in 1× PBS at pH 7.4) was then added to achieve the desired final concentration of ACE2 (or the equivalent dose for empty filaments). The mixture was incubated at 37°C for 45 min. Then 100 μL of the mixture was transferred to the target cells (293/ACE2/TMPRSS2, >90% confluency) in 24-well flat-bottom, tissue culture-treated plates (Falcon). Cells were incubated for an additional hour, and then the culture medium was changed to fresh medium. After an additional 48-h incubation, the Luciferase Assay System Kit (Promega) was used to analyze luciferase activity following the manufacturer's protocol. Experiments were performed with 6 technical repeats for each condition with a total of 3 biological repeats.

For assessment of the preventative effect of fACE2 (Figures 4E–4G), 293/ACE2/TMPRSS2 cells (>90% confluency) in a 24-well flat-bottom, tissue culture-treated plates were treated with 100 μL of Opti-MEM medium supplemented with 2% (v/v) FBS containing fACE2, ACE2, or empty ACE2-docking filaments (at 0.5 nM ACE2 dose or its equivalent in 1× PBS at pH 7.4). The treated cells were incubated at 37°C for set time points (ranging from 0 min to 8 h for all 3 groups and an additional 12–48 h for fACE2 and empty filament groups) before being challenged by addition of SARS-CoV-2 PsV (2 μL; titer, 1.7×10^{14} VP/mL). With the added PsV, cells were incubated for an additional hour, and then the culture medium was replaced with fresh medium. After an additional 48 h of incubation, luciferase activity was assessed with the Luciferase Assay System Kit (Promega) following the manufacturer's protocols. Experiments were performed with 6 technical repeats for each condition with a total of 3 biological repeats.

Animal studies

K18-hACE2 mice (male and female, 8–16 weeks old; The Jackson Laboratory Lab) were utilized for all animal experiments, which were approved by the Johns Hopkins University Animal Care and Use Committee. The animals were housed individually with access to food, water, and cage enrichment. After 1 week of acclimatization in the animal biosafety level 3 (ABSL-3) facility, the animals were anesthetized with ketamine and xylazine for intranasal inhalation of 20 μL of PBS, filament, rhACE2 (20 nM), or fACE2 (20 nM). Details regarding the methodology for preparing fACE2 and empty filaments before administration to mice are detailed in the above section "Aerosolization of ACE2-docking filaments and fACE2." 1 h after reagent administration, mice were inoculated with 1.5×10^5 50% tissue culture infectious dose (TCID50) of SARS-CoV-2 (USA-WA1/2020), delivered in 30 μL of DMEM. Mice were monitored daily for signs of sepsis or casualties. All mice were sacrificed 2 days after SARS-CoV-2 infection, and lung tissue was collected for analysis.

Histopathology and immunofluorescence

Formalin-fixed and paraffin-embedded tissue sections were stained with hematoxylin and eosin (H&E) or anti-SARS-CoV-2 N protein antibody (Novus Biologicals, NB100-56576; at a dilution of 1:200). Morphometric analyses were performed on affected lung tissues using ImageJ software (NIH, USA). At a minimum, three fields of view were obtained from each animal (n = 8 animals, 4 male and 4 female). Heat-induced epitope retrieval was conducted by heating slides to 95°C for 20 min in sodium citrate-based ER1 buffer (Leica Biosystems, Richmond, IL) before immunostaining. Immunostaining was performed using the Bond RX automated system (Leica Biosystems, Richmond, IL). Positive immunostaining was visualized using immunofluorescence (IF). Lung pathology score was calculated according to Zheng et al.[63] in brief as follows:

Neutrophil infiltration was evaluated by severity-based ordinal scoring:

0, within normal limits;
1, scattered PMNs sequestered in septa;
2, 1 plus solitary PMNs extravasated in airspaces;
3, plus small aggregates in vessel and airspaces.

Mononuclear infiltrates were evaluated by distribution-based ordinal scoring of 200× lung fields on a Nikon Eclipse 55i light microscope:

0, none;
1, uncommon detection in less than 5% of 200× lung fields;
2, detectable in up to 33% of 200× lung fields;
3, detectable in up to 33%–66% of 200× lung fields;
4, detectable in more than 66% of 200× lung fields.

Edema, hyaline membranes, necrotic cell debris, necrosis, and hemorrhage were not identified and not scored. Specimens were also assessed for inflammatory change, epithelial change, vascular change, edema, and hemorrhage.

qRT-PCR

Total mouse lung RNA was isolated using TRIzol reagent (Life Technologies) following the manufacturer's protocols. RNA was reverse transcribed using the iScript cDNA Synthesis Kit (Bio-Rad). SARS-CoV-2 N gene expression was determined by quantitative TaqMan PCR (Integrated DNA Technologies) following the protocols set by the manufacturer. The Ct values were normalized by the Ct value of a housekeeping gene, GAPDH (Bio-Rad). All other genes expression was determined by SyBr Green qRT-PCR as described in our previous publication.[65]

SUPPLEMENTAL INFORMATION

Supplemental information can be found online at https://doi.org/10.1016/j.matt.2022.11.027.

ACKNOWLEDGMENTS

The work reported here is supported by the National Institutes of Health (1R2AI14932101, 3R21AI149321-01S1, and 1R01AI148446-01A1) and a Fisher Center Discovery Program grant. E.K.L. is supported by NIH training grant K12 GM123914 01A1. We thank Maggie Lowman, Morgan Craney, and Amanda J. Wong for technical support; Dr. David Hackam for consultation with respect to

experimental design; the Integrated Imaging Center (IIC) at The Johns Hopkins University for use of the TEM facility; and the Johns Hopkins University Department of Chemistry Mass Spectroscopy facility for use of the MALDI-TOF instrument. Aspects of the schematics depicted in Figure 4 were created with BioRender.com.

AUTHOR CONTRIBUTIONS

H.J. and H.C. conceived the idea of delivering soluble ACE2 with supramolecular polymers. H.J. and H.C. guided experiments and provided insight into final interpretation of the results. C.F.A. conceived design of ACE2-docking supramolecular filaments; synthesized materials; designed and performed material characterization, docking optimization, and *in vitro* cell studies; and interpreted the results. Q.W. executed *in vivo* studies. D.S. aided design and execution of docking optimization experiments and interpretation of the results. B.S. and K.J.F. aided in execution of *in vitro* cell studies. E.K.J. aided in design of and executed binding affinity experiments and interpretation of the results. J.B.S. aided in design and interpretation of binding affinity results. C.-Y.C. aided execution of *in vivo* experiments. J.V. provided oversight of *in vivo* ASBL3 experiments. C.F.B. processed and analyzed pathology samples. A.P. provided viral stocks and oversight of *in vitro* and *in vivo* experiments. C.F.A. analyzed all data, and H.J. analyzed *in vivo* data. C.F.A., H.J., and H.C. co-wrote the manuscript. All authors discussed results and contributed to the manuscript write-up.

DECLARATION OF INTERESTS

The authors declare no competing interests.

Received: August 10, 2022
Revised: October 11, 2022
Accepted: November 16, 2022
Published: December 12, 2022

REFERENCES

1. Wang, C., Horby, P.W., Hayden, F.G., and Gao, G.F. (2020). A novel coronavirus outbreak of global health concern. Lancet *395*, 470–473. https://doi.org/10.1016/S0140-6736(20)30185-9.

2. Zhou, P., Yang, X.-L., Wang, X.-G., Hu, B., Zhang, L., Zhang, W., Si, H.-R., Zhu, Y., Li, B., Huang, C.-L., et al. (2020). A pneumonia outbreak associated with a new coronavirus of probable bat origin. Nature *579*, 270–273. https://doi.org/10.1038/s41586-020-2012-7.

3. Tay, M.Z., Poh, C.M., Rénia, L., MacAry, P.A., and Ng, L.F.P. (2020). The trinity of COVID-19: immunity, inflammation and intervention. Nat. Rev. Immunol. *20*, 363–374. https://doi.org/10.1038/s41577-020-0311-8.

4. Wang, Y., Zhang, D., Du, G., Du, R., Zhao, J., Jin, Y., Fu, S., Gao, L., Cheng, Z., Lu, Q., et al. (2020). Remdesivir in adults with severe COVID-19: a randomised, double-blind, placebo-controlled, multicentre trial. Lancet *395*, 1569–1578. https://doi.org/10.1016/S0140-6736(20)31022-9.

5. Williamson, B.N., Feldmann, F., Schwarz, B., Meade-White, K., Porter, D.P., Schulz, J., van Doremalen, N., Leighton, I., Yinda, C.K., Pérez-Pérez, L., et al. (2020). Clinical benefit of remdesivir in rhesus macaques infected with SARS-CoV-2. Nature *585*, 273–276. https://doi.org/10.1038/s41586-020-2423-5.

6. Hacisuleyman, E., Hale, C., Saito, Y., Blachere, N.E., Bergh, M., Conlon, E.G., Schaefer-Babajew, D.J., DaSilva, J., Muecksch, F., Gaebler, C., et al. (2021). Vaccine breakthrough infections with SARS-CoV-2 variants. N. Engl. J. Med. *384*, 2212–2218. https://doi.org/10.1056/NEJMoa2105000.

7. To, K.K.-W., Hung, I.F.-N., Ip, J.D., Chu, A.W.-H., Chan, W.-M., Tam, A.R., Fong, C.H.-Y., Yuan, S., Tsoi, H.-W., Ng, A.C.-K., et al. (2020). Coronavirus disease 2019 (COVID-19) Re-infection by a phylogenetically distinct severe acute respiratory syndrome coronavirus 2 strain confirmed by whole genome sequencing. Clin. Infect. Dis. *73*, e2946–e2951. https://doi.org/10.1093/cid/ciaa1275.

8. Li, Q., Wu, J., Nie, J., Zhang, L., Hao, H., Liu, S., Zhao, C., Zhang, Q., Liu, H., Nie, L., et al. (2020). The impact of mutations in SARS-CoV-2 spike on viral infectivity and antigenicity. Cell *182*, 1284–1294.e9. https://doi.org/10.1016/j.cell.2020.07.012.

9. Zhang, L., Jackson, C.B., Mou, H., Ojha, A., Peng, H., Quinlan, B.D., Rangarajan, E.S., Pan, A., Vanderheiden, A., Suthar, M.S., et al. (2020). SARS-CoV-2 spike-protein D614G mutation increases virion spike density and infectivity. Nat. Commun. *11*, 6013. https://doi.org/10.1038/s41467-020-19808-4.

10. Kuba, K., Imai, Y., Rao, S., Gao, H., Guo, F., Guan, B., Huan, Y., Yang, P., Zhang, Y., Deng, W., et al. (2005). A crucial role of angiotensin converting enzyme 2 (ACE2) in SARS coronavirus–induced lung injury. Nat. Med. *11*, 875–879. https://doi.org/10.1038/nm1267.

11. Lan, J., Ge, J., Yu, J., Shan, S., Zhou, H., Fan, S., Zhang, Q., Shi, X., Wang, Q., Zhang, L., and Wang, X. (2020). Structure of the SARS-CoV-2 spike receptor-binding domain bound to the ACE2 receptor. Nature *581*, 215–220. https://doi.org/10.1038/s41586-020-2180-5.

12. Hoffmann, M., Kleine-Weber, H., Schroeder, S., Kruger, N., Herrler, T., Erichsen, S., Schiergens, T.S., Herrler, G., Wu, N.H., Nitsche, A., et al. (2020). SARS-CoV-2 cell entry depends on ACE2 and TMPRSS2 and is blocked by a clinically proven protease inhibitor. Cell *181*, 271–280.e8. https://doi.org/10.1016/j.cell.2020.02.052.

13. Yan, R., Zhang, Y., Li, Y., Xia, L., Guo, Y., and Zhou, Q. (2020). Structural basis for the recognition of SARS-CoV-2 by full-length

human ACE2. Science *367*, 1444. https://doi.org/10.1126/science.abb2762.

14. Zoufaly, A., Poglitsch, M., Aberle, J.H., Hoepler, W., Seitz, T., Traugott, M., Grieb, A., Pawelka, E., Laferl, H., Wenisch, C., et al. (2020). Human recombinant soluble ACE2 in severe COVID-19. Lancet Respir. Med. *8*, 1154–1158. https://doi.org/10.1016/S2213-2600(20)30418-5.

15. Yeung, M.L., Teng, J.L.L., Jia, L., Zhang, C., Huang, C., Cai, J.-P., Zhou, R., Chan, K.-H., Zhao, H., Zhu, L., et al. (2021). Soluble ACE2-mediated cell entry of SARS-CoV-2 via interaction with proteins related to the renin-angiotensin system. Cell *184*, 2212–2228.e12. https://doi.org/10.1016/j.cell.2021.02.053.

16. Chan, K.K., Dorosky, D., Sharma, P., Abbasi, S.A., Dye, J.M., Kranz, D.M., Herbert, A.S., and Procko, E. (2020). Engineering human ACE2 to optimize binding to the spike protein of SARS coronavirus 2. Science *369*, 1261. https://doi.org/10.1126/science.abc0870.

17. Glasgow, A., Glasgow, J., Limonta, D., Solomon, P., Lui, I., Zhang, Y., Nix, M.A., Rettko, N.J., Zha, S., Yamin, R., et al. (2020). Engineered ACE2 receptor traps potently neutralize SARS-CoV-2. Proc. Natl. Acad. Sci. USA *117*, 28046. https://doi.org/10.1073/pnas.2016093117.

18. Monteil, V., Kwon, H., Prado, P., Hagelkrüys, A., Wimmer, R.A., Stahl, M., Leopoldi, A., Garreta, E., Hurtado del Pozo, C., Prosper, F., et al. (2020). Inhibition of SARS-CoV-2 infections in engineered human tissues using clinical-grade soluble human ACE2. Cell *181*, 905–913.e7. https://doi.org/10.1016/j.cell.2020.04.004.

19. Jia, H. (2016). Pulmonary angiotensin-converting enzyme 2 (ACE2) and inflammatory lung disease. Shock *46*, 239–248.

20. Jia, H., Neptune, E., and Cui, H. (2020). Targeting ACE2 for COVID-19 therapy: opportunities and challenges. Am. J. Respir. Cell Mol. Biol. *64*, 416–425. https://doi.org/10.1165/rcmb.2020-0322PS.

21. Liu, P., Wysocki, J., Souma, T., Ye, M., Ramirez, V., Zhou, B., Wilsbacher, L.D., Quaggin, S.E., Batlle, D., and Jin, J. (2018). Novel ACE2-Fc chimeric fusion provides long-lasting hypertension control and organ protection in mouse models of systemic renin angiotensin system activation. Kidney Int. *94*, 114–125. https://doi.org/10.1016/j.kint.2018.01.029.

22. Haschke, M., Schuster, M., Poglitsch, M., Loibner, H., Salzberg, M., Bruggisser, M., Penninger, J., and Krahenbuhl, S. (2013). Pharmacokinetics and pharmacodynamics of recombinant human angiotensin-converting enzyme 2 in healthy human subjects. Clin. Pharmacokinet. *52*, 783–792. https://doi.org/10.1007/s40262-013-0072-7.

23. Zhang, Q., Honko, A., Zhou, J., Gong, H., Downs, S.N., Vasquez, J.H., Fang, R.H., Gao, W., Griffiths, A., and Zhang, L. (2020). Cellular nanosponges inhibit SARS-CoV-2 infectivity. Nano Lett. *20*, 5570–5574. https://doi.org/10.1021/acs.nanolett.0c02278.

24. Rao, L., Xia, S., Xu, W., Tian, R., Yu, G., Gu, C., Pan, P., Meng, Q.F., Cai, X., Qu, D., et al. (2020). Decoy nanoparticles protect against COVID-19 by concurrently adsorbing viruses and inflammatory cytokines. Proc. Natl. Acad. Sci. USA *117*, 27141–27147. https://doi.org/10.1073/pnas.2014352117.

25. Li, Z., Wang, Z., Dinh, P.-U.C., Zhu, D., Popowski, K.D., Lutz, H., Hu, S., Lewis, M.G., Cook, A., Andersen, H., et al. (2021). Cell-mimicking nanodecoys neutralize SARS-CoV-2 and mitigate lung injury in a non-human primate model of COVID-19. Nat. Nanotechnol. *16*, 942–951. https://doi.org/10.1038/s41565-021-00923-2.

26. Yu, Y.-C., Berndt, P., Tirrell, M., and Fields, G.B. (1996). Self-assembling amphiphiles for construction of protein molecular architecture. J. Am. Chem. Soc. *118*, 12515–12520. https://doi.org/10.1021/ja9627656.

27. Hartgerink, J.D., Beniash, E., and Stupp, S.I. (2001). Self-assembly and mineralization of peptide-amphiphile nanofibers. Science *294*, 1684. https://doi.org/10.1126/science.1063187.

28. Hartgerink, J.D., Beniash, E., and Stupp, S.I. (2002). Peptide-amphiphile nanofibers: a versatile scaffold for the preparation of self-assembling materials. Proc. Natl. Acad. Sci. USA *99*, 5133. https://doi.org/10.1073/pnas.072699999.

29. Zhang, P., Cheetham, A.G., Lin, Y.-a., and Cui, H. (2013). Self-assembled tat nanofibers as effective drug carrier and transporter. ACS Nano *7*, 5965–5977. https://doi.org/10.1021/nn401667z.

30. Hudalla, G.A., Sun, T., Gasiorowski, J.Z., Han, H., Tian, Y.F., Chong, A.S., and Collier, J.H. (2014). Gradated assembly of multiple proteins into supramolecular nanomaterials. Nat. Mater. *13*, 829–836. https://doi.org/10.1038/nmat3998.

31. Lee, S.S., Hsu, E.L., Mendoza, M., Ghodasra, J., Nickoli, M.S., Ashtekar, A., Polavarapu, M., Babu, J., Riaz, R.M., Nicolas, J.D., et al. (2015). Gel scaffolds of BMP-2-binding peptide amphiphile nanofibers for spinal arthrodesis. Adv. Healthc. Mater. *4*, 131–141. https://doi.org/10.1002/adhm.201400129.

32. Miller, S.E., Yamada, Y., Patel, N., Suárez, E., Andrews, C., Tau, S., Luke, B.T., Cachau, R.E., and Schneider, J.P. (2019). Electrostatically driven guanidinium interaction domains that control hydrogel-mediated protein delivery in vivo. ACS Cent. Sci. *5*, 1750–1759. https://doi.org/10.1021/acscentsci.9b00501.

33. Li, Y., Lock, L.L., Wang, Y., Ou, S.-H., Stern, D., Schön, A., Freire, E., Xu, X., Ghose, S., Li, Z.J., and Cui, H. (2018). Bioinspired supramolecular engineering of self-assembling immunofibers for high affinity binding of immunoglobulin G. Biomaterials *178*, 448–457. https://doi.org/10.1016/j.biomaterials.2018.04.032.

34. Krishnamurthy, S., Wohlford-Lenane, C., Kandimalla, S., Sartre, G., Meyerholz, D.K., Théberge, V., Hallée, S., Duperré, A.-M., Del'Guidice, T., Lepetit-Stoffaes, J.-P., et al. (2019). Engineered amphiphilic peptides enable delivery of proteins and CRISPR-associated nucleases to airway epithelia. Nat. Commun. *10*, 4906. https://doi.org/10.1038/s41467-019-12922-y.

35. Si, Y., Tian, Q., Zhao, F., Kelly, S.H., Shores, L.S., Camacho, D.F., Sperling, A.I., Andrade, M.S., Collier, J.H., and Chong, A.S. (2020). Adjuvant-free nanofiber vaccine induces in situ lung dendritic cell activation and T_H17 responses. Sci. Adv. *6*, eaba0995. https://doi.org/10.1126/sciadv.aba0995.

36. Anderson, C.F., Chakroun, R.W., Su, H., Mitrut, R.E., and Cui, H. (2019). Interface-enrichment-induced instability and drug-loading-enhanced stability in inhalable delivery of supramolecular filaments. ACS Nano *13*, 12957–12968. https://doi.org/10.1021/acsnano.9b05556.

37. Geng, Y., Dalhaimer, P., Cai, S., Tsai, R., Tewari, M., Minko, T., and Discher, D.E. (2007). Shape effects of filaments versus spherical particles in flow and drug delivery. Nat. Nanotechnol. *2*, 249–255. https://doi.org/10.1038/nnano.2007.70.

38. Edwards, D.A., Hanes, J., Caponetti, G., Hrkach, J., Ben-Jebria, A., Eskew, M.L., Mintzes, J., Deaver, D., Lotan, N., and Langer, R. (1997). Large porous particles for pulmonary drug delivery. Science *276*, 1868. https://doi.org/10.1126/science.276.5320.1868.

39. Lai, S.K., Hanlon, D.E., Harrold, S., Man, S.T., Wang, Y.-Y., Cone, R., and Hanes, J. (2007). Rapid transport of large polymeric nanoparticles in fresh undiluted human mucus. Proc. Natl. Acad. Sci. USA *104*, 1482. https://doi.org/10.1073/pnas.0608611104.

40. Lock, L.L., Reyes, C.D., Zhang, P., and Cui, H. (2016). Tuning cellular uptake of molecular probes by rational design of their assembly into supramolecular nanoprobes. J. Am. Chem. Soc. *138*, 3533–3540. https://doi.org/10.1021/jacs.6b00073.

41. Chung, E.J., Mlinar, L.B., Sugimoto, M.J., Nord, K., Roman, B.B., and Tirrell, M. (2015). In vivo biodistribution and clearance of peptide amphiphile micelles. Nanomed. Nanotechnol. Biol. Med. *11*, 479–487. https://doi.org/10.1016/j.nano.2014.08.006.

42. Champion, J.A., and Mitragotri, S. (2006). Role of target geometry in phagocytosis. Proc. Natl. Acad. Sci. USA *103*, 4930–4934. https://doi.org/10.1073/pnas.0600997103.

43. Towler, P., Staker, B., Prasad, S.G., Menon, S., Tang, J., Parsons, T., Ryan, D., Fisher, M., Williams, D., Dales, N.A., et al. (2004). ACE2 X-ray structures reveal a large hinge-bending motion important for inhibitor binding and catalysis. J. Biol. Chem. *279*, 17996–18007. https://doi.org/10.1074/jbc.M311191200.

44. Li, Y., Lock, L.L., Mills, J., Ou, B.S., Morrow, M., Stern, D., Wang, H., Anderson, C.F., Xu, X., Ghose, S., et al. (2020). Selective capture and recovery of monoclonal antibodies by self-assembling supramolecular polymers of high affinity for protein binding. Nano Lett. *20*, 6957–6965. https://doi.org/10.1021/acs.nanolett.0c01297.

45. Huang, L., Sexton, D.J., Skogerson, K., Devlin, M., Smith, R., Sanyal, I., Parry, T., Kent, R., Enright, J., Wu, Q.L., et al. (2003). Novel peptide inhibitors of angiotensin-converting enzyme 2. J. Biol. Chem. *278*, 15532–15540. https://doi.org/10.1074/jbc.M212934200.

46. Behanna, H.A., Donners, J.J.J.M., Gordon, A.C., and Stupp, S.I. (2005). Coassembly of amphiphiles with opposite peptide polarities

into nanofibers. J. Am. Chem. Soc. *127*, 1193–1200. https://doi.org/10.1021/ja044863u.

47. Amin, M., Sorour, M.K., and Kasry, A. (2020). Comparing the binding interactions in the receptor binding domains of SARS-CoV-2 and SARS-CoV. J. Phys. Chem. Lett. *11*, 4897–4900. https://doi.org/10.1021/acs.jpclett.0c01064.

48. Zhang, S., Greenfield, M.A., Mata, A., Palmer, L.C., Bitton, R., Mantei, J.R., Aparicio, C., de la Cruz, M.O., and Stupp, S.I. (2010). A self-assembly pathway to aligned monodomain gels. Nat. Mater. *9*, 594–601. https://doi.org/10.1038/nmat2778.

49. Adjei, A., and Gupta, P. (1994). Pulmonary delivery of therapeutic peptides and proteins. J. Contr. Release *29*, 361–373. https://doi.org/10.1016/0168-3659(94)90081-7.

50. Hertel, S.P., Winter, G., and Friess, W. (2015). Protein stability in pulmonary drug delivery via nebulization. Adv. Drug Deliv. Rev. *93*, 79–94. https://doi.org/10.1016/j.addr.2014.10.003.

51. Berndt, P., Fields, G.B., and Tirrell, M. (1995). Synthetic lipidation of peptides and amino acids: monolayer structure and properties. J. Am. Chem. Soc. *117*, 9515–9522.

52. Choi, H.S., Ashitate, Y., Lee, J.H., Kim, S.H., Matsui, A., Insin, N., Bawendi, M.G., Semmler-Behnke, M., Frangioni, J.V., and Tsuda, A. (2010). Rapid translocation of nanoparticles from the lung airspaces to the body. Nat. Biotechnol. *28*, 1300–1303. https://doi.org/10.1038/nbt.1696.

53. Anderson, C.F., Chakroun, R.W., Grimmett, M.E., Domalewski, C.J., Wang, F., and Cui, H. (2022). Collagen-binding peptide-enabled supramolecular hydrogel design for improved organ adhesion and sprayable therapeutic delivery. Nano Lett. *22*, 4182–4191. https://doi.org/10.1021/acs.nanolett.2c00967.

54. Liu, Q., Guan, J., Qin, L., Zhang, X., and Mao, S. (2020). Physicochemical properties affecting the fate of nanoparticles in pulmonary drug delivery. Drug Discov. Today *25*, 150–159. https://doi.org/10.1016/j.drudis.2019.09.023.

55. Geiser, M., and Kreyling, W.G. (2010). Deposition and biokinetics of inhaled nanoparticles. Part. Fibre Toxicol. *7*, 2. https://doi.org/10.1186/1743-8977-7-2.

56. Pedersen, S.F., and Ho, Y.-C. (2020). SARS-CoV-2: a storm is raging. J. Clin. Investig. *130*, 2202–2205. https://doi.org/10.1172/JCI137647.

57. Antinori, S., Bonazzetti, C., Gubertini, G., Capetti, A., Pagani, C., Morena, V., Rimoldi, S., Galimberti, L., Sarzi-Puttini, P., and Ridolfo, A.L. (2020). Tocilizumab for cytokine storm syndrome in COVID-19 pneumonia: an increased risk for candidemia? Autoimmun. Rev. *19*, 102564. https://doi.org/10.1016/j.autrev.2020.102564.

58. Zhang, X., Tan, Y., Ling, Y., Lu, G., Liu, F., Yi, Z., Jia, X., Wu, M., Shi, B., Xu, S., et al. (2020). Viral and host factors related to the clinical outcome of COVID-19. Nature *583*, 437–440. https://doi.org/10.1038/s41586-020-2355-0.

59. Lagunas-Rangel, F.A., and Chávez-Valencia, V. (2020). High IL-6/IFN-γ ratio could be associated with severe disease in COVID-19 patients. J. Med. Virol. *92*, 1789–1790. https://doi.org/10.1002/jmv.25900.

60. Abers, M.S., Delmonte, O.M., Ricotta, E.E., Fintzi, J., Fink, D.L., de Jesus, A.A.A., Zarember, K.A., Alehashemi, S., Oikonomou, V., Desai, J.V., et al. (2021). An immune-based biomarker signature is associated with mortality in COVID-19 patients. JCI Insight *6*, e144455. https://doi.org/10.1172/jci.insight.144455.

61. Ghazavi, A., Ganji, A., Keshavarzian, N., Rabiemajd, S., and Mosayebi, G. (2021). Cytokine profile and disease severity in patients with COVID-19. Cytokine *137*, 155323. https://doi.org/10.1016/j.cyto.2020.155323.

62. Kim, M.-H., Salloum, S., Wang, J.Y., Wong, L.P., Regan, J., Lefteri, K., Manickas-Hill, Z., Gao, C., Li, J.Z., Sadreyev, R.I., et al. (2021). Type I, II, and III interferon signatures correspond to coronavirus disease 2019 severity. J. Infect. Dis. *224*, 777–782. https://doi.org/10.1093/infdis/jiab288.

63. Zheng, J., Wong, L.-Y.R., Li, K., Verma, A.K., Ortiz, M.E., Wohlford-Lenane, C., Leidinger, M.R., Knudson, C.M., Meyerholz, D.K., McCray, P.B., and Perlman, S. (2021). COVID-19 treatments and pathogenesis including anosmia in K18-hACE2 mice. Nature *589*, 603–607. https://doi.org/10.1038/s41586-020-2943-z.

64. Johnson, M.C., Lyddon, T.D., Suarez, R., Salcedo, B., LePique, M., Graham, M., Ricana, C., Robinson, C., Ritter, D.G., and Simon, V. (2020). Optimized pseudotyping conditions for the SARS-COV-2 spike glycoprotein. J. Virol. *94*. e01062-e01020. https://doi.org/10.1128/JVI.01062-20.

65. Sodhi, C.P., Nguyen, J., Yamaguchi, Y., Werts, A.D., Lu, P., Ladd, M.R., Fulton, W.B., Kovler, M.L., Wang, S., Prindle, T., et al. (2019). A dynamic variation of pulmonary ACE2 is required to modulate neutrophilic inflammation in response to *Pseudomonas aeruginosa* lung infection in mice. J. Immunol. *203*, 3000. https://doi.org/10.4049/jimmunol.1900579.

Matter, Volume *6*

Supplemental information

Supramolecular filaments for concurrent ACE2 docking and enzymatic activity silencing enable coronavirus capture and infection prevention

Caleb F. Anderson, Qiong Wang, David Stern, Elissa K. Leonard, Boran Sun, Kyle J. Fergie, Chang-yong Choi, Jamie B. Spangler, Jason Villano, Andrew Pekosz, Cory F. Brayton, Hongpeng Jia, and Honggang Cui

Supplemental Items

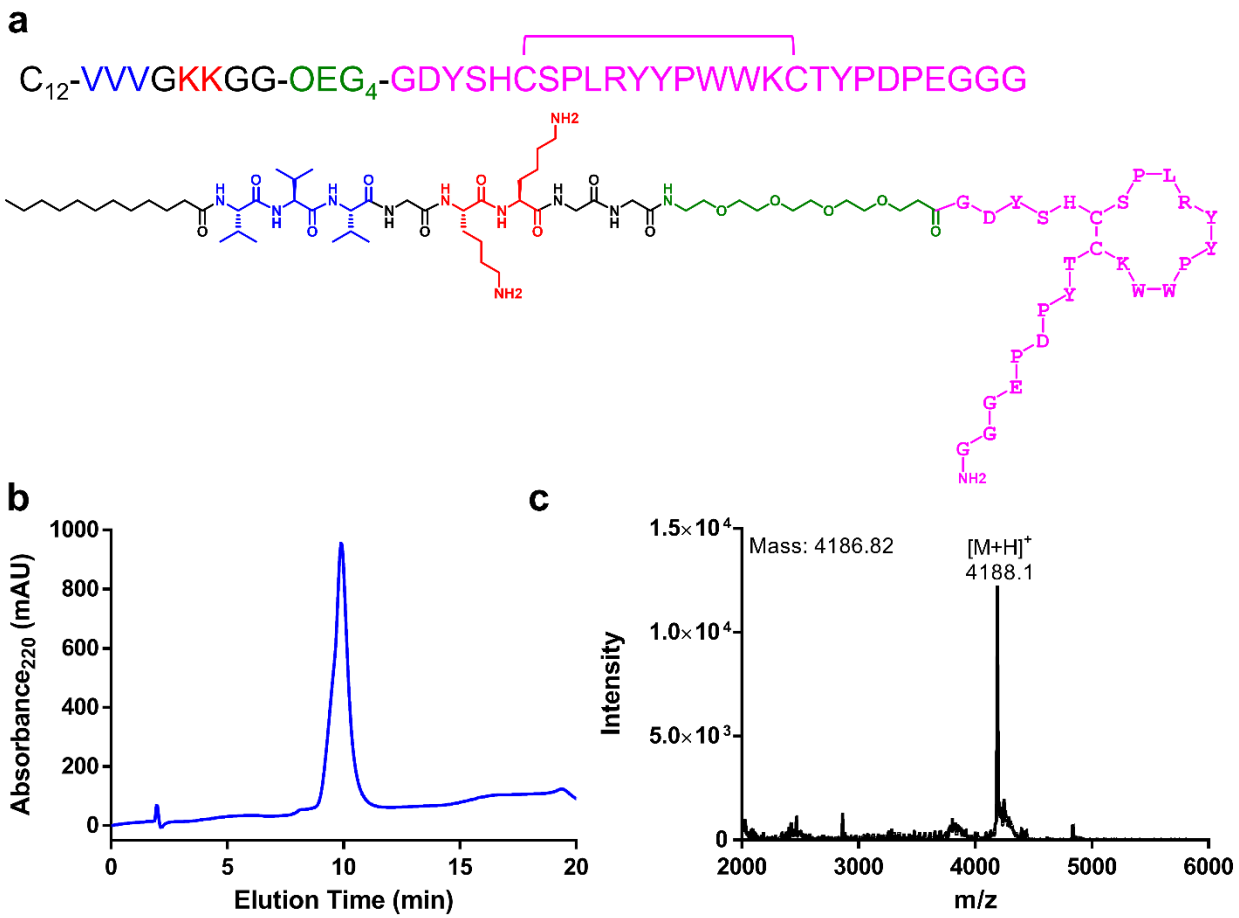

Figure S1. Molecular design and characterization of Ligand PA. (**a**) Full peptide sequence and chemical structure of Ligand, showing full sequence of ACE2-inhibiting peptide ligand, DX600, through which ACE2 specifically binds to the PA molecule. Full chemical structure of Ligand PA is detailed in Figure S21. (**b**) Analytical RP-HPLC chromatogram of Ligand, showing high purity. (**c**) MALDI-ToF mass spectrum of Ligand, where peak at 4188.1 corresponds to $[M+H]^+$ (compared to calculated molecular weight of 4186.82).

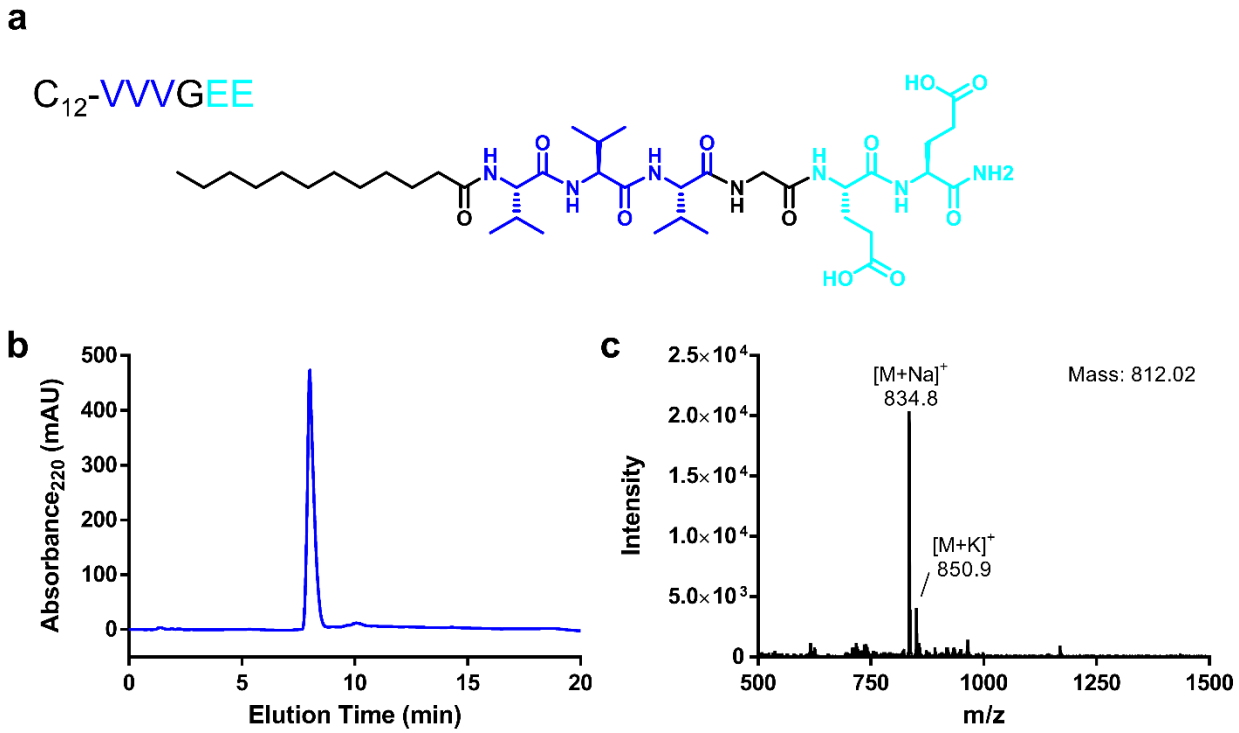

Figure S2. Molecular design and characterization of Filler PA. (**a**) Full peptide sequence and chemical structure of Filler. (**b**) Analytical RP-HPLC chromatogram of Filler, showing high purity. (**c**) MALDI-ToF mass spectrum of Filler, where peaks at 834.8 and 850.9 correspond to $[M+Na]^+$ and $[M+K]^+$, respectively (compared to calculated molecular weight of 812.02).

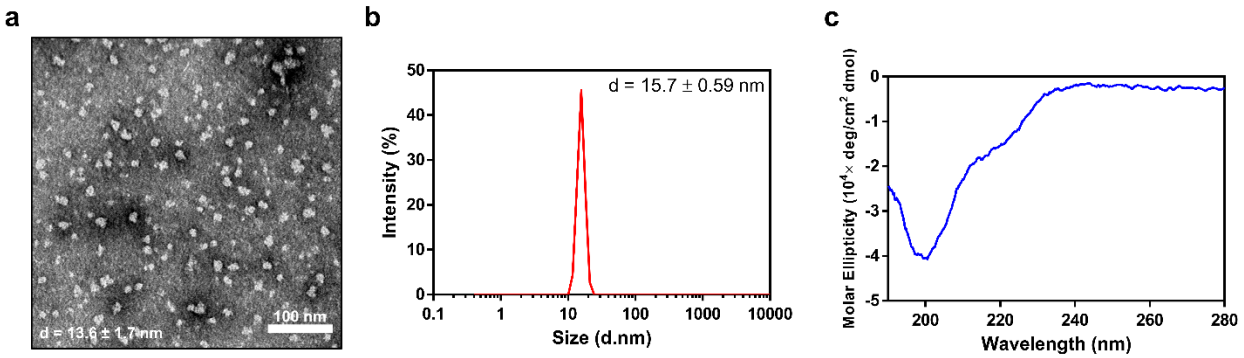

Figure S3. Self-assembly characterization of Ligand PA alone. (**a**) Representative transmission electron microscopy image of Ligand at 200 μM in MilliQ water (pH = 7.4) after aging for 24 h, showing assembly into spherical aggregates. Diameter represented as mean ± SD (n = 35). (**b**) Dynamic light scattering measurement of Ligand at 100 μM in PBS (pH = 7.4) after aging for 24 h, confirming presence of spherical aggregates observed with TEM. Diameter measurement presented as mean ± SD (n = 3). (**c**) Circular dichroism measurement of Ligand spherical aggregates at 100 μM in MilliQ water (pH = 7.4) after aging for 24 h, showing random coil secondary structure as evidenced by negative peak around 200 nm.

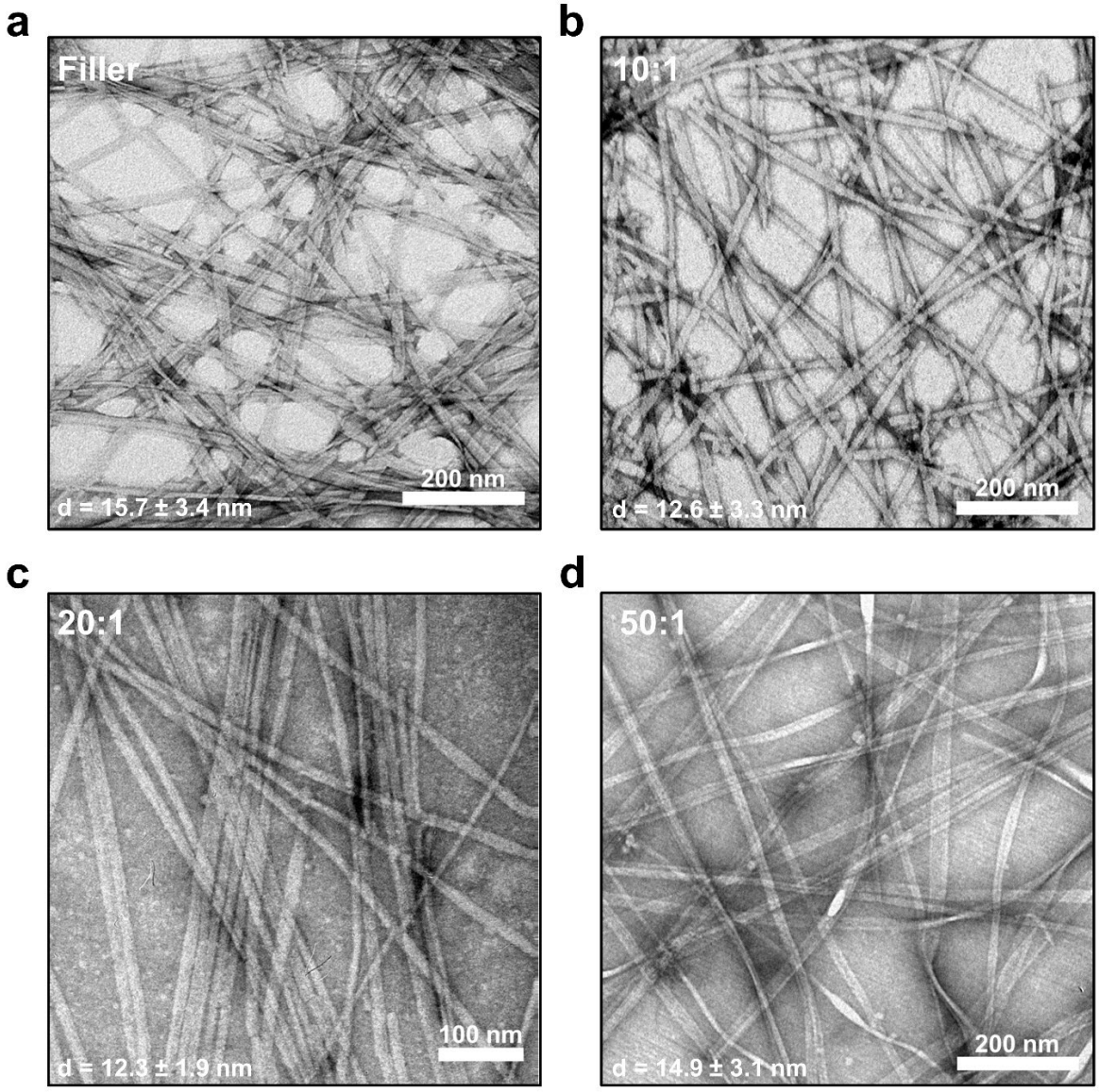

Figure S4. Self-assembly characterization of the co-assembly of Filler and Ligand at varying molar ratios. Representative transmission electron microscopy (TEM) image of (**a**) Filler at 500 μM, in MilliQ water (pH = 7.4) after aging for 24 h, showing assembly into ribbon-like filaments. Diameter represented as mean ± SD (n = 35). Representative TEM image of (**b**) 10:1, (**c**) 20:1, and (**d**) 50:1 molar ratio of Filler:Ligand with 50 μM Ligand in MilliQ water (pH = 7.4) after aging for 24 h, showing co-assembly into ribbon-like filaments for every ratio studied. Diameters represented as mean ± SD (n = 35).

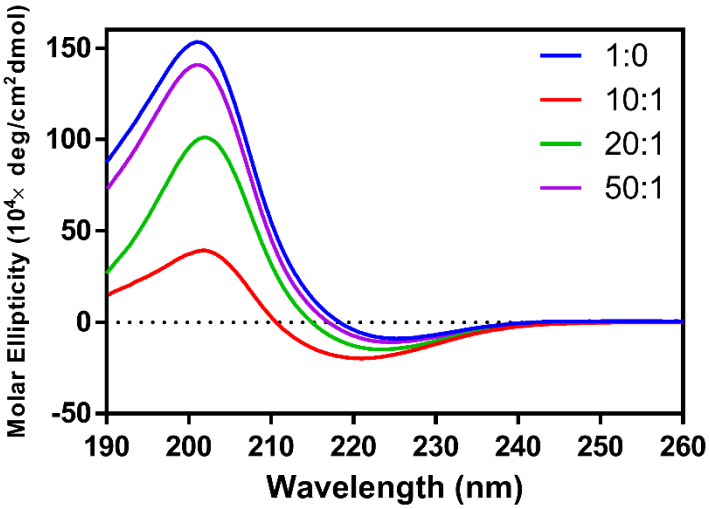

Figure S5. Circular dichroism (CD) spectra of the co-assembly of Filler and Ligand at varying molar ratios, ranging from 1:0 to 50:1 Filler:Ligand. All spectra are representative of samples in MilliQ water at pH = 7.4 after immediate dilution to 100 μM before scanning. The CD spectra of 1:0 shows an intense positive peak around 207 nm and red-shifted negative peak at ~226 nm, which is suggestive of β-turn character in addition to more linear β-sheet character.[1,2] With increasing content of Ligand in the supramolecular structures, the β-turn content decreases and CD spectra represent more typical linear β-sheet character with stronger negative peak at ~220 nm and weaker, blue-shifted positive peak at ~202 nm. Spectrum for each sample represents average of 3 scans.

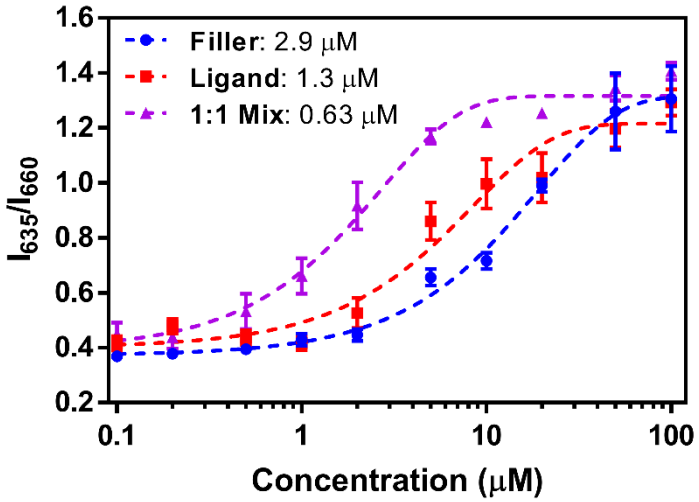

Figure S6. Determination of critical micelle concentration (CMC) for Filler, Ligand, and their co-assembly in MilliQ water (pH = 7.4) using Nile Red assay. The fluorescence intensity maximum is shifted from 660 nm to 635 nm as the Nile Red dye becomes encapsulated within the supramolecular structures of the PAs. The presented CMC values are calculated as the transition point between the two wavelengths. Data are presented as mean ± SD (n = 3).

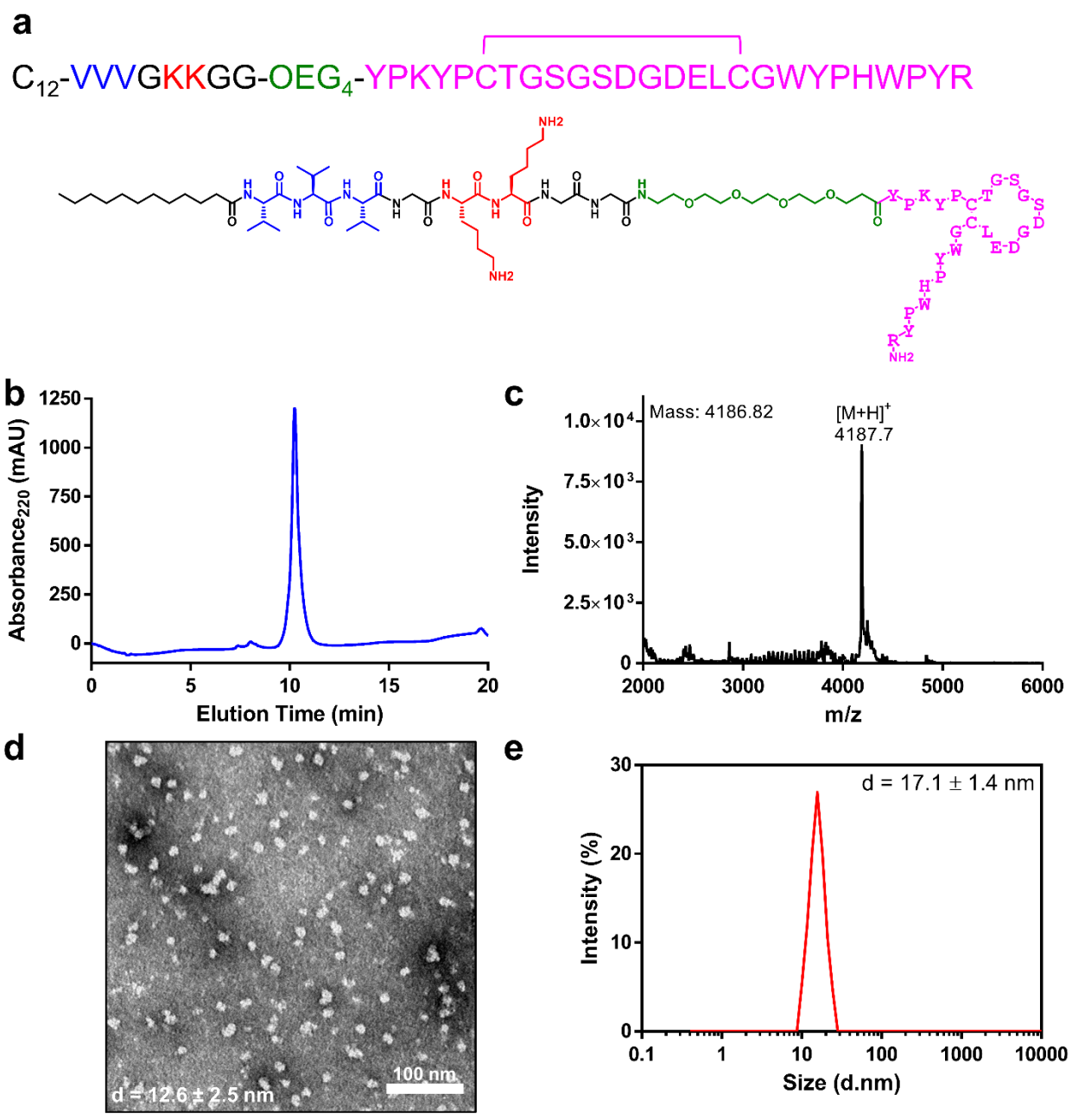

Figure S7. Molecular design, characterization, and self-assembly behavior of sLigand PA. (**a**) Full peptide sequence and chemical structure of sLigand, showing scrambled sequence of ACE2-inhibiting peptide ligand, DX600, where loop is maintained in the same position, but the amino acid sequence was randomly shuffled otherwise. (**b**) Analytical RP-HPLC chromatogram of sLigand, showing high purity. (**c**) MALDI-ToF mass spectrum of sLigand, where peak at 4187.7 corresponds to $[M+H]^+$ (compared to calculated molecular weight of 4186.82). (**d**) Representative transmission electron microscopy image of sLigand at 200 μM in MilliQ water (pH = 7.4) after aging for 24 h, showing assembly into spherical aggregates. Diameter represented as mean ± SD (n = 35). (**e**) Dynamic light scattering measurement of sLigand at 100 μM in PBS (pH = 7.4) after aging for 24 h, confirming presence of spherical aggregates observed with TEM. Diameter measurement presented as mean ± SD (n = 3).

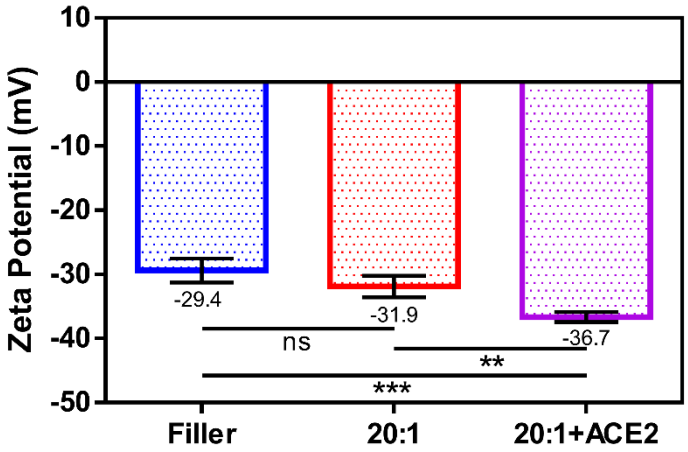

Figure S8. Zeta potential measurements of Filler alone and ACE2-docking filaments (20:1 molar ratio Filler:Ligand) before and after ACE2 addition. Filament zeta potential is negligibly impacted by incorporation of Ligand, emphasizing role of Filler in regulating surface charge. Large drop in zeta potential after addition of ACE2 suggests complexation at the surface of the supramolecular filaments. Data are presented as mean ± SD (ns $p > 0.5$, ** $p < 0.01$, *** $p < 0.001$, one-way ANOVA with Tukey's post hoc test, n = 3).

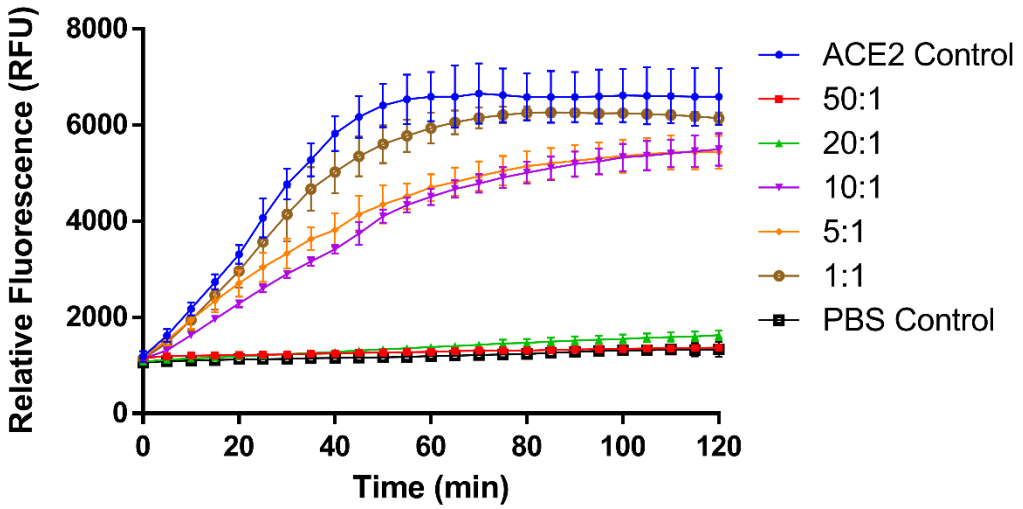

Figure S9. Kinetic measurement of evolved fluorescence intensity of activity probe by ACE2 cleavage in the presence of ACE2-docking filaments. The concentration of Filler within the filaments is varied while holding Ligand and ACE2 concentration constant, showing greater inhibition of ACE2 with increased spacing. Data presented as mean ± SD (n = 3).

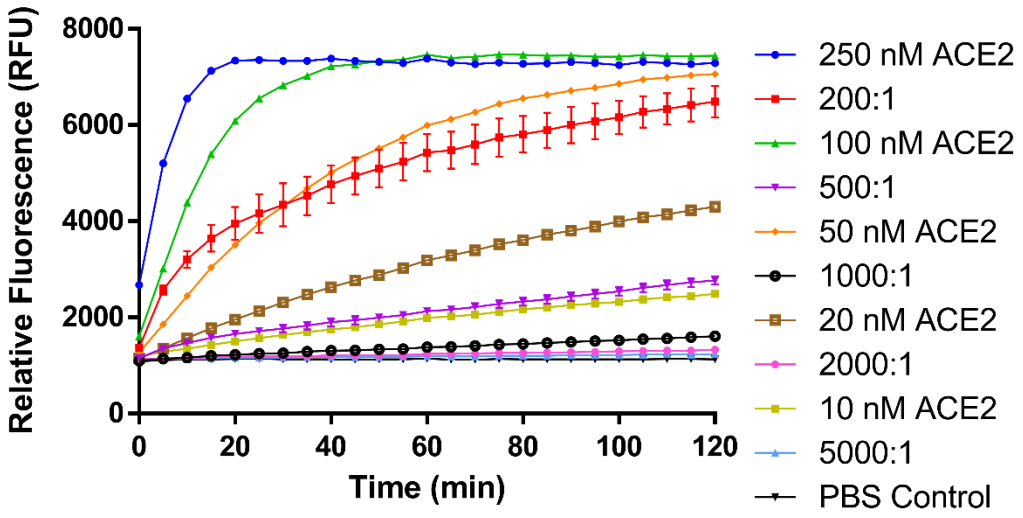

Figure S10. Kinetic measurement of evolved fluorescence intensity of activity probe by ACE2 cleavage in the presence of ACE2-docking filaments. The molar ratio of Filler to Ligand is held constant (20:1) while the Ligand:enzyme ratio is varied, showing greater inhibition with greater Ligand to ACE2 ratios. Data presented as mean ± SD (n = 3).

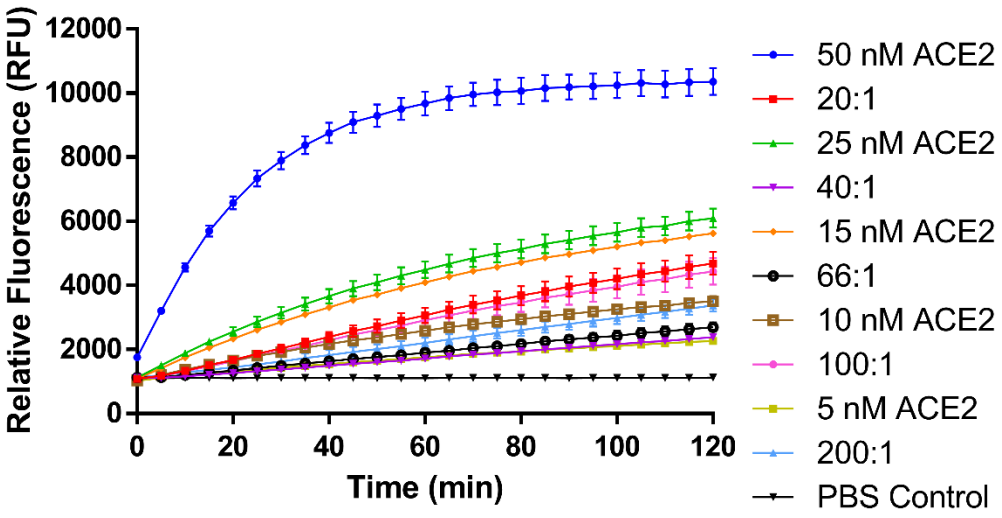

Figure S11. Kinetic measurement of evolved fluorescence intensity of activity probe by ACE2 cleavage in the presence of ACE2-docking filaments. Both the concentration of Filler and the Ligand:enzyme ratio are fixed while the concentration of Ligand is varied, showing greater inhibition of ACE2 with increasing Ligand concentration. Data presented as mean ± SD (n = 3).

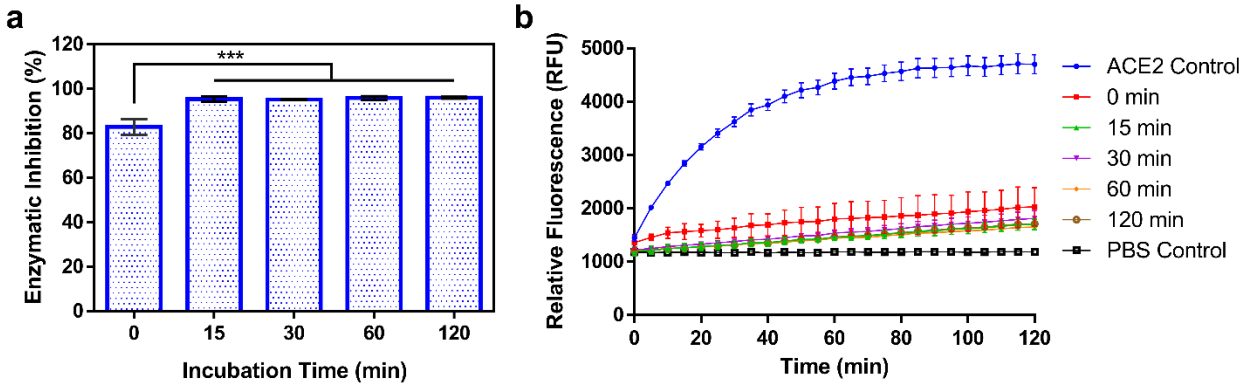

Figure S12. Influence of incubation time on docking efficiency of ACE2 to ACE2-docking filament surfaces. (**a**) Enzymatic inhibition (calculated based on relative reaction initial velocities compared to free ACE2) of ACE2 after incubation with ACE2-docking filaments for set time before assessment with activity assay, showing maximum docking achieved after 15 min. Data presented as mean ± SD (***$p < 0.001$, ns $p > 0.05$ amongst groups 15 min and later; one-way ANOVA with Tukey's post hoc test, n = 3). (**b**) Kinetic measurement of evolved fluorescence of activity probe by ACE2 cleavage in the presence of ACE2-docking filaments after incubation for varied times before assessment with activity assay, showing a minimum of 15 min is required to achieve maximum inhibition of ACE2 activity. Data presented as mean ± SD (n = 3).

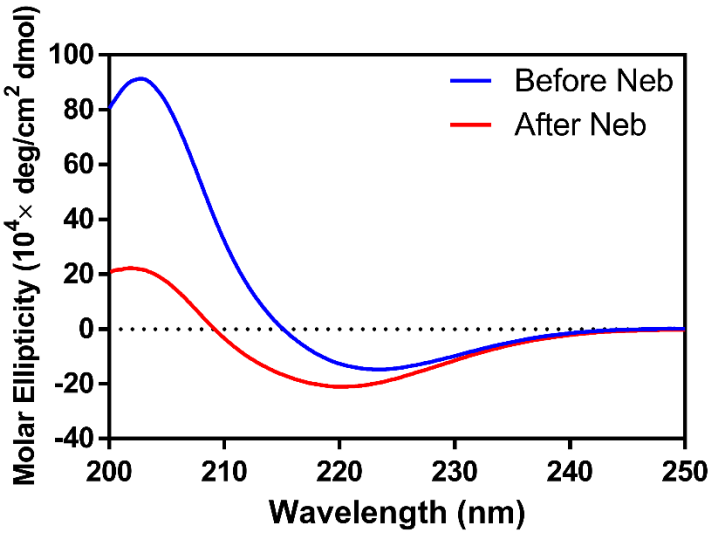

Figure S13. Circular dichroism (CD) spectra of **fACE2** before and after nebulization (1 mM in PBS at pH = 7.4 with immediate dilution to 100 μM before running sample), showing retention of β-sheet character (negative peaks around 220 nm) after nebulization but also a reduction in signal intensity reflective of disrupted hydrogen-bonding. Spectra represent average of 3 scans.

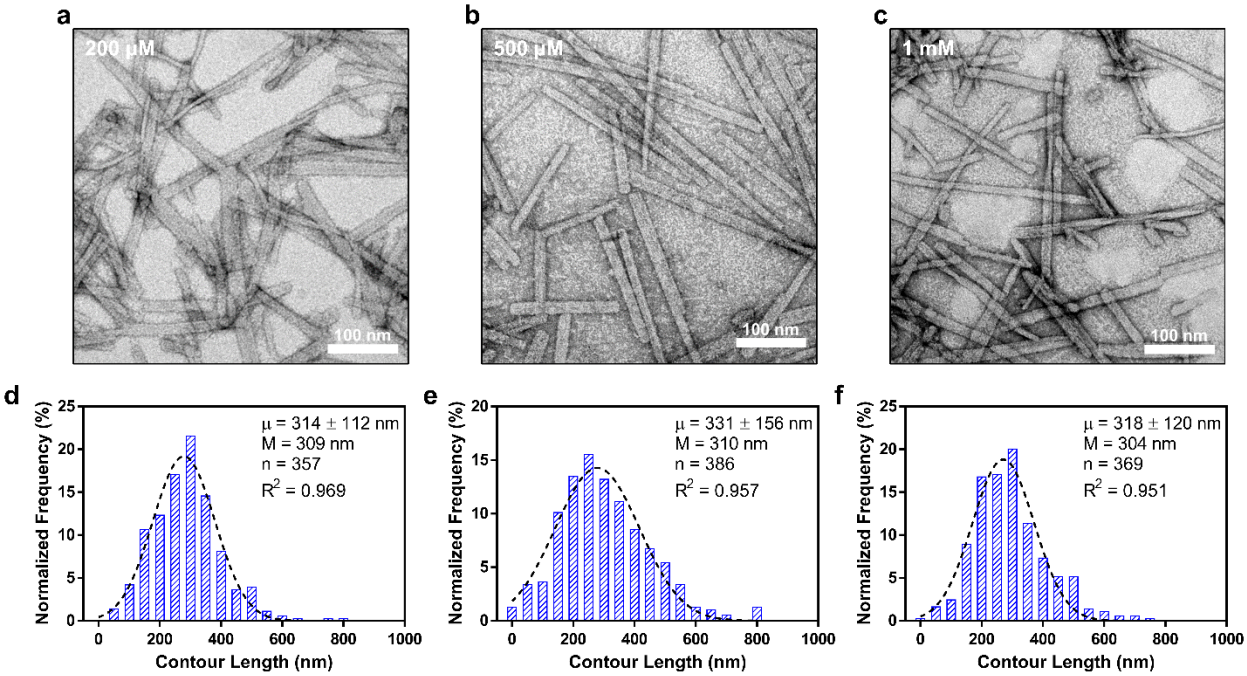

Figure S14. Post-nebulization filament fragmentation of various formulation concentrations of **fACE2** in PBS (pH = 7.4). Representative transmission electron microscopy images of **fACE2** at (**a**) 200 µM, (**b**) 500 µM, and (**c**) 1 mM after nebulization, showing reduced filament length. Population size distributions for the contour lengths of observed filaments after jet nebulization for each formulation concentration of **fACE2** (20 bins, 50 nm each) from TEM images, where µ represents average contour length given as mean ± SD alongside median (M) measured length: (**d**) 200 µM (n = 357 analyzed filaments), (**e**) 500 µM (n = 386 analyzed filaments), and (**f**) 1 mM (n = 369 analyzed filaments). Dotted lines represent fit of data to a Gaussian distribution. For average contour length of each starting concentration, ns $p > 0.05$ by one-way ANOVA with Tukey's post hoc test, highlighting the similarity of the size distributions.

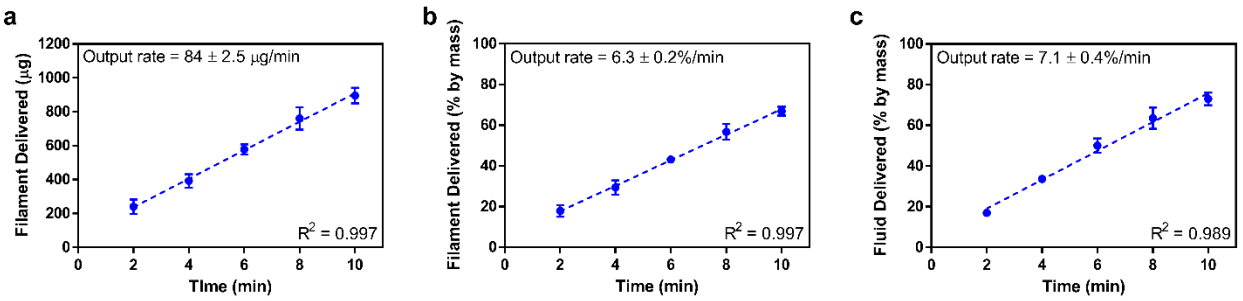

Figure S15. Release profiles of **fACE2** from a jet nebulizer over the course of a 10 min nebulization event (500 µM formulation in PBS at pH = 7.4). Release of **fACE2** by (**a**) total mass emitted (µg), (**b**) fraction of loaded dose (% by mass), and (**c**) weight of formulation fluid (% by mass), highlighting linear profile. Data presented as mean ± SD (n = 3); dashed lines represent results of linear regression analysis. For output rates of filament mass and fluid mass (%), ns $p > 0.05$ by two-tailed unpaired *t*-test with Welch's correction, though slightly lower output rate of filaments may reflect heterogeneity in aerosol droplet concentration over the course of a nebulization event.

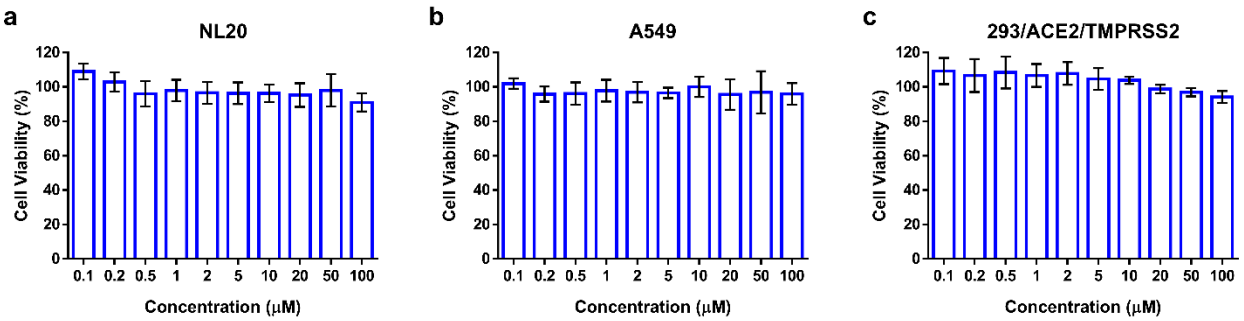

Figure S16. Cytotoxicity of ACE2-docking filaments after 48 h incubation concentrations (ranging from 0.1 to 100 μM) for (**a**) NL20, (**b**) A549, and (**c**) 293/ACE2/TMPRSS2 cells lines as determined by MTT assay. Data presented as mean ± SD (n = 3 independent experiments).

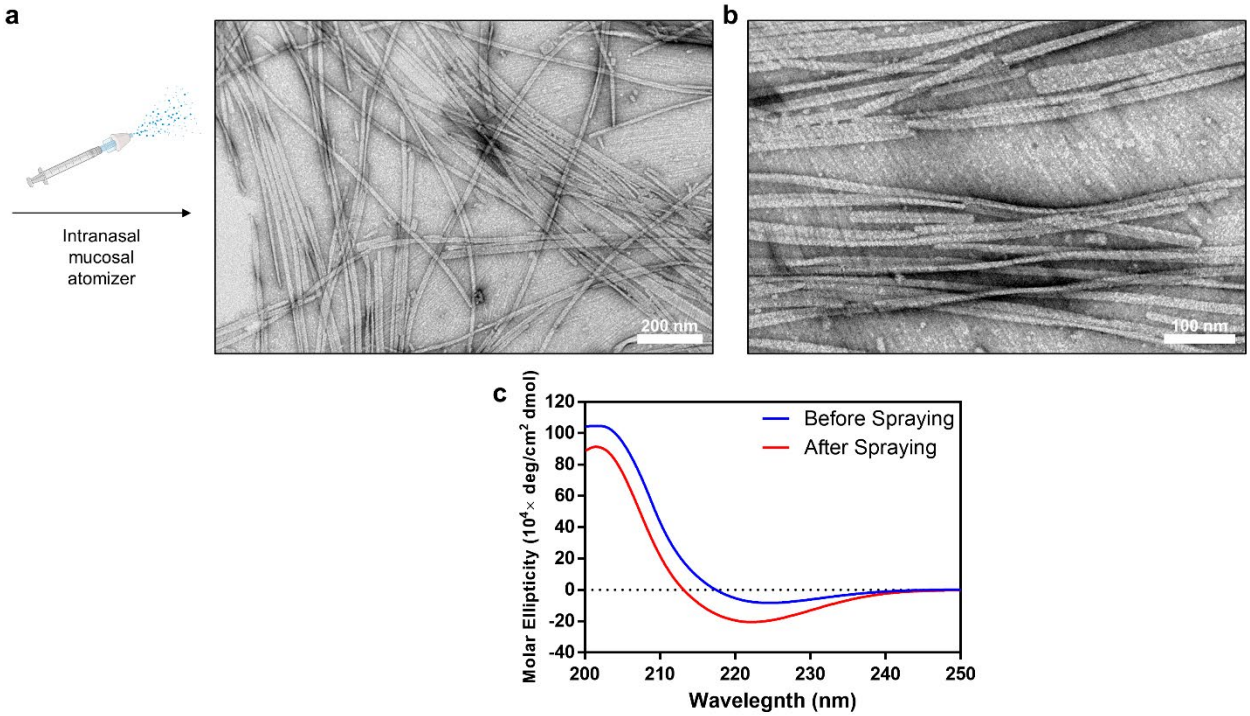

Figure S17. Filament characterization of **fACE2** after administration with an intranasal mucosal atomizer. Representative (**a**) low- and (**b**) high-magnification transmission electron microscopy images of **fACE2** (500 μM in PBS, pH = 7.4) post-atomization, showing instances of filament fragmentation and alignment, likely due to shear forces. (**c**) Circular dichroism (CD) spectra of **fACE2** before and after atomization (500 μM in PBS at pH = 7.4 with immediate dilution to 100 μM before running sample), showing retention of β-sheet character (negative peaks around 220 nm) after nebulization but also a reduction in signal intensity reflective of disrupted hydrogen-bonding. Spectra represent average of 3 scans.

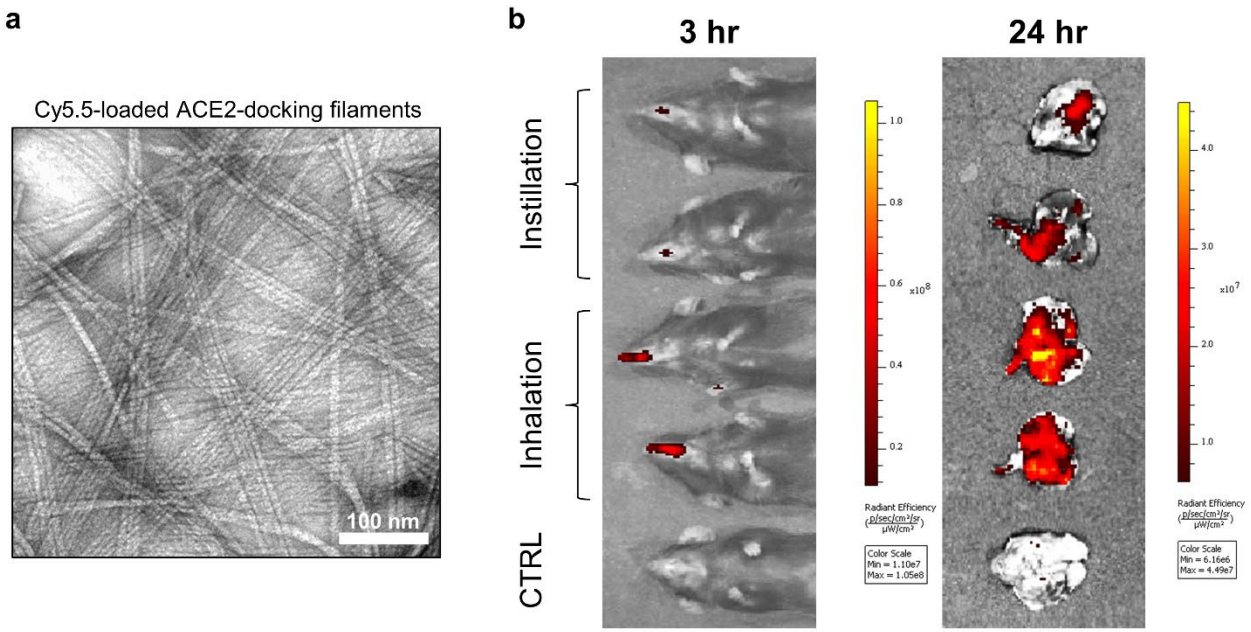

Figure S18. *In vivo* lung distribution study of ACE2-docking filaments in K18-hACE2 mice after inhalation administration. (**a**) Representative transmission electron microscopy image of near-infrared dye Cyanine 5.5-loaded ACE2-docking filaments (500 μM in PBS, pH = 7.4) used for visualizing filament distribution. (**b**) In Vivo Imaging System (IVIS) fluorescence imaging of K18-hACE2 mice after administration of atomized Cy5.5-loaded ACE2-docking filaments (in PBS, 10 nM equivalent ACE2 dose (molar ratio 20:1 Filler:Ligand filaments, 200 μM)) either via intratracheal instillation or intranasal inhalation (control = intranasal inhalation of PBS only). Images on left shows retention of filaments in nasal cavity of mice 3 h post-administration. Lungs harvested from mice 24 h post-administration of filaments shows strong fluorescence signal from filaments throughout lung tissues, suggesting enhanced retention (n = 2 mice per group, 1 control). Experiments were repeated twice with similar results.

Note S1 on Figure S18:

The observed differences in filament retention and distribution between the intranasal inhalation and intratracheal instillation groups can likely be attributed to the differences in these routes of administration. With intratracheal instillation, intubated mice receive filaments directly to the lungs, bypassing the upper respiratory tract and delivering a bolus dose. This can lead to heterogenous distribution patterns of lung retention. In contrast, intranasal inhalation delivers filaments through the physiological route, where breathing filament-bearing droplets leads to deeper and more spread distribution within the lungs. A greater portion of lung tissue is observed to contain fluorescence signal for the inhalation group, whereas the instillation group shows fluorescence localized closer to the trachea.[3-5]

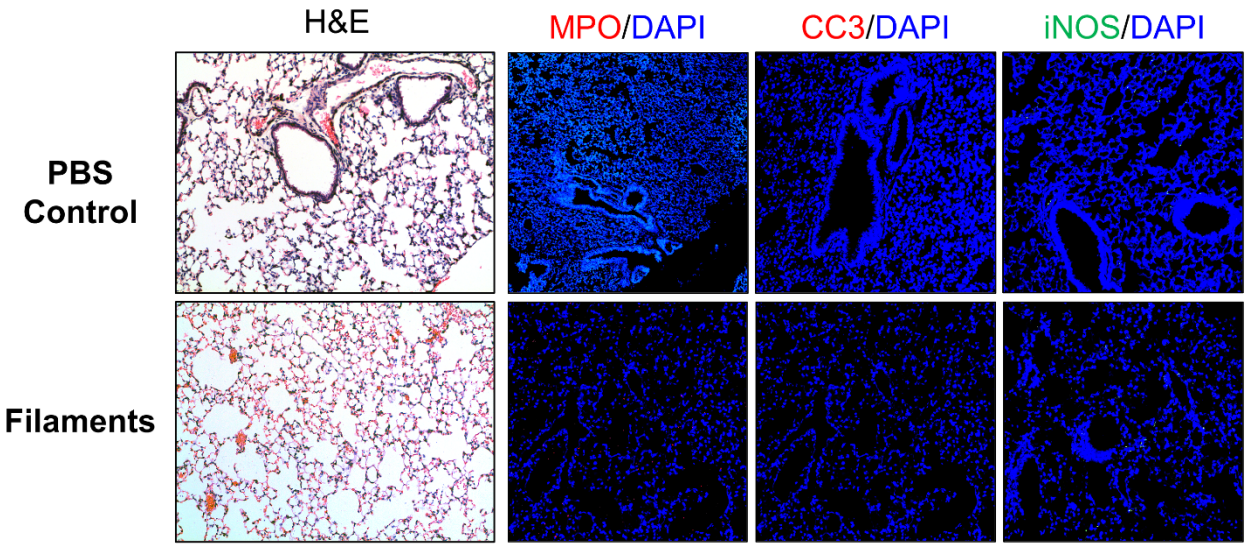

Figure S19. Histology of lung tissue sections of K18-hACE2 mice 24 h after administration of atomized Cy5.5-loaded ACE2-docking filaments (in PBS, 10 nM ACE2 equivalent dose (molar ratio 20:1 Filler:Ligand filaments, 200 μM)) via intranasal inhalation. Compared to PBS-only control, hematoxylin and eosin (H&E) staining and immunofluorescence show no obvious sign of lung cell apoptosis, inflammation, or neutrophil infiltration from treatment with ACE2-docking filaments, suggesting filaments are relatively biocompatible and safe delivery vehicles for ACE2 (neutrophil invasion, myeloperoxidase (anti-MPO antibody), red; apoptosis marker, cleaved-caspase 3 (anti-CC3 antibody), red; pro-inflammatory cytokine production, inducible nitric oxide synthase (anti-iNOS antibody), green; cell nuclei, DAPI, blue). Experiments were repeated twice with similar results.

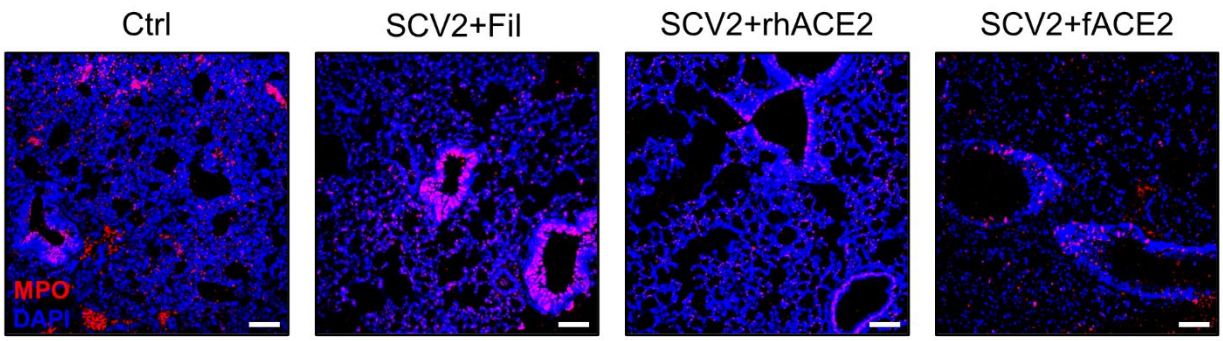

Figure S20. Immunofluorescence staining of harvested mouse lung tissue sections after treatment and SARS-CoV-2 inoculation, assessing neutrophil infiltration. Neutrophil invasion is markedly decreased with treatment with fACE2, indicating alleviated lung inflammation and related pathology (myeloperoxidase (anti-MPO antibody), red; cell nuclei (DAPI), blue). Scale bars represent 50 μm.

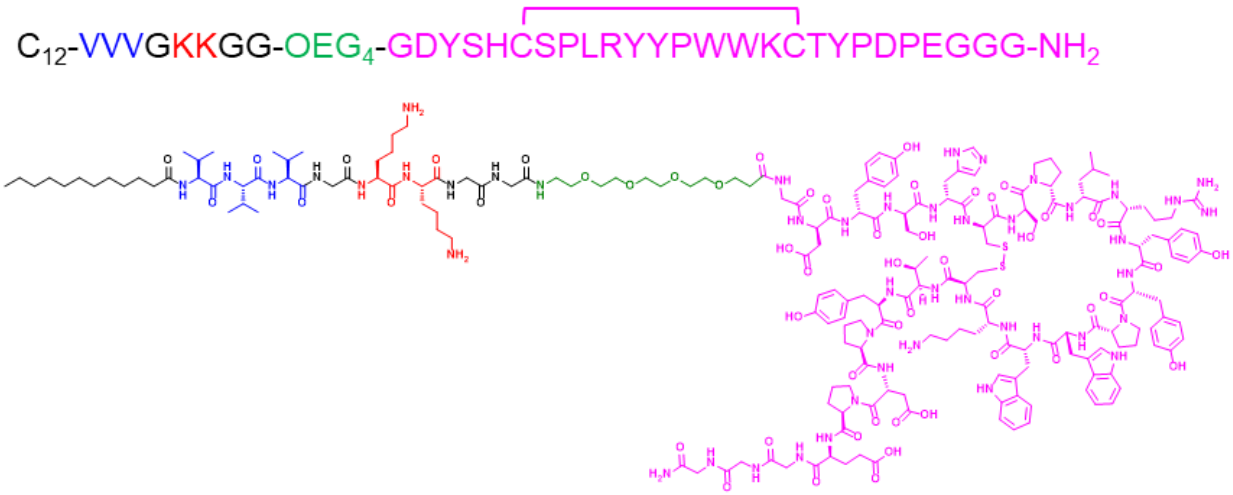

Figure S21. Full chemical structure of the Ligand PA design.

Supplemental Experimental Procedures

Peptide amphiphile synthesis and purification

All peptide amphiphiles (PAs) studied were synthesized using standard 9-fluorenylmethoxycarbonyl (Fmoc) solid phase peptide synthesis techniques. All three PAs (Filler, Ligand, sLigand) were synthesized onto Rink amide 4-methylbenzhydrylamine (MBHA) resin (100-200 mesh, 0.53 mmol/g). All Fmoc deprotections were performed with 20% 4-methylpiperidine in *N*,*N*-dimethylformamide (DMF) for 15 minutes, repeated once. After Fmoc removal, each amino acid coupling was performed at a 4:4:6 molar ratio of the Fmoc-protected amino acid, O-benzotrizole-*N*,*N*,*N*',*N*'-tetramethyluronium hexafluorophosphate (HBTU), and *N*,*N*-diisopropylethylamine (DIEA) in DMF and shook for 2 h for the coupling reaction. For Ligand and sLigand molecules, Fmoc-PEG_4-COOH was conjugated to peptide chain at a molar ratio of 2:2:3 to resin of Fmoc-PEG_4-COOH, HBTU, and DIEA in DMF and shaken for 24 h. After final amino acid conjugation and Fmoc deprotection, lauric acid (C_{12} alkyl chain) was coupled to the peptide in a 4:4:6 molar ratio to resin of lauric acid, HBTU, and DIEA in DMF and shaken overnight. For Ligand and sLigand molecules, Acm deprotection and disulfide bond formation (from Cys(Acm) residues of the DX600 peptide ligand segment of the design) was conducted with thallium trifluoroacetate (2 equivalents) in DMF and swirled with resin on ice for 2 h; resin was subsequently washed with methanol (MeOH), DMF, and then MeOH again. Completed PAs were cleaved from their resin by addition of a 10 mL mixture of 95% v/v trifluoroacetic acid (TFA), 2.5% v/v triisopropylsilane (TIS), and 2.5% v/v water and shaken for 3 h. After cleavage, the TFA solution was collected and excess TFA removed via evaporation, and subsequently the product was precipitated with cold diethyl ether and then dried under vacuum overnight.

Each crude PA solid was dissolved in a water and acetonitrile (ACN) mixture containing 0.1% v/v TFA for Ligand and sLigand molecules and 0.1% v/v ammonium hydroxide (NH_4OH) for Filler. A Varian ProStar Model 325 (Agilent Technologies, Santa Clara, CA) reverse-phase high performance liquid chromatography (RP-HPLC) was employed to purify the PA molecules using mobile phases of water and ACN at matching acidic or basic phase. PAs were separated from impurities by preparative RP-HPLC using a Varian PLRP-S column (C_{18}, 100 Å, 10 µm, 150 × 25 mm) with a flow rate of 20 mL/min, 10 mL injections, and monitoring at 220 nm for peptide absorbance for all molecules. For Filler, the eluent gradient was run linearly from 30% to 45% ACN over 20 min, and for Ligand and sLigand, the gradient was run linearly from 25% to 55% ACN over 30 min. The collected fractions were analyzed by matrix-assisted laser desorption/ionization time of flight (MALDI-ToF) mass spectrometry to isolate fractions containing the molecules of interest. Correct fractions were combined, and excess ACN was removed via rotary evaporation. Samples were then lyophilized using a FreeZone -105°C 4.5L freeze dryer (Labconco, Kansas City, MO). Re-characterization of the purified PA powders were conducted by analytical RP-HPLC and MALDI-ToF. Product purity was assessed with analytical RP-HPLC using a Varian Pursuit XRs column (C_{18}, 5 µm, 150 × 4.6 mm) with a flow rate of 1 mL/min, 20 µL injections, and monitoring at 220 nm. Purity was assessed with a linear gradient of 5% to 95% ACN over 15 min, where area under the curve (AUC) of the PA peak relative to total AUC of all peaks was used to confirm purity greater than 95% (purity data for each molecule shown in **Figures S1, S2, S7**). The redissolved PAs were calibrated, aliquoted into cryo-vials, re-lyophilized, and stored at -20°C freezer for future use.[6-8]

MALDI-ToF Mass Spectroscopy

Matrix-assisted laser desorption/ionization time of flight (MALDI-ToF) mass spectroscopy was used to analyze the molecular weights for all synthesized PA molecules with a BrukerAutoflex III MALDI-ToF instrument (Bruker, Billerica, MA). Samples were prepared by first depositing a 2 µL droplet of sinapic acid matrix solution (10 mg/mL in 1:1 v/v water:ACN with 0.05% TFA; Sigma-Aldrich) onto an MTP 384 ground steel target plate (Bruker, Billerica, MA). The matrix was allowed to dry for 5-10 min, and then 1 µL of aqueous PA solution was added to the corresponding spot of dried matrix followed by the immediate addition of 1 µL of matrix solution and mixed. The spots were allowed to dry for 10-20 min before analyzing on the instrument, where samples were irradiated with a 355 nm UV laser and analyzed in the reflectron mode. Representative MALDI-ToF mass spectra for each of the PAs studied are shown in **Figures S1, S2, S7**.

Dynamic Light Scattering (DLS)

Spherical micelle/aggregate solutions of Ligand and sLigand dissolved in PBS at pH = 7.4 were diluted to 100 μM and placed in a UV-transparent disposable cuvettes (0.5 mL, 45 × 12 mm, special plastic, Sarstedt, Nümbrecht, Germany). Samples were analyzed on a Malvern Zetasizer Nano-ZS ZEN3600 (Malvern Panalytical) at 25°C. Three runs were collected for each sample (10 scans/measurement) and averaged.

Circular Dichroism (CD)

Solutions of the supramolecular systems were diluted to 100 μM, added to a 1 mm path length quartz UV-Vis absorption cell (Thermo Fisher Scientific, Pittsburgh, PA), and then analyzed with a Jasco J-710 spectropolarimeter (JASCO, Easton, MD). Each sample was analyzed by three repeated scans from wavelengths of 190 to 300 nm (for samples in water) or from 200 to 300 nm (for samples in PBS). The high tension (HT) values were monitored during run collection (ranging from 200 to 600 V) to ensure no scattering artifacts were present in the representative spectra. A background spectrum (water or PBS) was obtained and subtracted from sample spectra. All obtained spectra were averaged over 3 scans and converted from ellipticity (mdeg) to molar ellipticity ($deg \cdot cm^2 \cdot dmol^{-1}$). For nebulized samples, sample concentration post-nebulization was determined using a standard curve derived from analytical HPLC runs to account for solvent evaporation that may occur during aerosol formation.

Critical Micelle Concentration (CMC) Measurements

Using a Nile Red assay, the CMC of each PA monomer (Filler and Ligand) and their co-assembly (1:1 molar ratio) was determined. Nile Red dye intensely fluoresces within hydrophobic environments but is strongly quenched and red-shifted in aqueous environments. Thus, when mixed with PAs at a concentration exceeding the CMC, Nile Red will embed within the hydrophobic core and emit a strong fluorescence signal. A 500 μM stock solution of Nile Red was prepared in acetone, and 10 μL of the stock was added to microcentrifuge tubes. Acetone was evaporated off in the dark. Solutions of the samples (500 μL, water) were added to the tubes at varied concentrations and were aged for 2 days in the dark at room temperature. Samples were added to a quartz micro fluorometer cell (0.7 mL, 10 mm pathlength, Starna Cells, Atascadero, CA), and at an excitation wavelength of 550 nm, five parallel emission spectra were recorded at a wavelength range of 580 to 720 nm on a Duetta UV-Vis-NIR spectrofluorometer (HORIBA Scientific). The emission intensity ratio for each run at 635 nm (emission maximum of Nile Red in a hydrophobic environment) to 660 nm (emission maximum of Nile Red in a hydrophilic environment) was plotted against tested concentrations to obtain a transition curve from which CMC was determined.

Bio-Layer Interferometry (BLI)

Biotinylated human ACE2 (NP_068576.1, Sino Biological) was immobilized to streptavidin-coated tips (Pall Life Sciences) for analysis on an Octet Red96 bio-layer interferometry (BLI) instrument (Sartorius). Less than 5 signal units (nm) of ACE2 was immobilized to minimize mass transfer effects. PBSA (PBS pH 7.2 containing 1% BSA) was used for all dilutions and as dissociation buffer. Tips were exposed to serial dilutions of Ligand PA and sLigand PA in a 96-well plate for 300 s. Dissociation was then measured for 150 s. Surface regeneration for all interactions was conducted using 15 s exposure to 0.1 M glycine pH 3.0 solution. Normalized equilibrium binding curves were obtained by plotting the response value at the end of the association phase for each sample dilution, dividing by the molecular weight of each ligand, and normalizing to the maximum value. Equilibrium binding curves were fitted and K_D values determined using GraphPad Prism data analysis software v9.0, assuming all binding interactions to be first order. Experiments were performed twice with similar results.

Zeta Potential Measurements

All zeta potential measurements were conducted for samples in PBS (pH = 7.4) at 25°C. Samples were added to a disposable folded capillary zeta cell (DTS1070, Malvern Panalytical) and analyzed using a Malvern Zetasizer Nano-ZS ZEN3600 (Malvern Panalytical). For analysis of mixtures, ACE2 was added

to solutions of Ligand, sLigand, and 20:1 docking filaments (molar ratio of Filler:Ligand) at an equal volume, such that a final concentration of 50 nM ACE2 was achieved, alongside 50 μM Ligand or sLigand. Three repeated runs were performed for each sample (20 measurements/run) and then averaged. The intensity-averaged zeta potential for mixtures of samples was calculated based on the average derived count rate and zeta potential measured for the individual components and their respective volume fractions after mixing assuming no interaction. This theoretical value was compared to measured experimental values of the systems after ACE2 addition to invalidate the "no interaction" assumption; these calculations were conducted only for Ligand and sLigand spherical aggregates with ACE2, since filaments are anisotropic and more polydisperse and Zetasizer software uses models for fitting best suited to spherical particles.[9,10]

Intensity-averaged zeta potential: ζ_{AB}
For a mixture of 2 components: component A (volume fraction, α; scattering intensity/derived count rate, int_A; zeta potential, ζ_A) and component B (volume fraction, β; scattering intensity/derived count rate, int_B; zeta potential, ζ_B)

$$\alpha + \beta = 1$$

$$\zeta_{AB} = \frac{\alpha \cdot int_A \cdot \zeta_A + \beta \cdot int_B \cdot \zeta_B}{\alpha \cdot int_A + \beta \cdot int_B}$$

For ACE2 + Ligand (equal volume fractions): calculated ζ_{AB} = -17.6 mV, measured -25.1 mV
For ACE2 + sLigand (equal volume fractions): calculated ζ_{AB} = -19.0 mV, measured -19.2 mV

Cell Lines

The A549 human alveolar epithelial adenocarcinoma cell line was supplied from ATCC (CCL-185) and grown in F12-K media supplemented with 10% v/v fetal bovine serum (FBS) and 1% v/v penicillin/streptomycin (Gibco, Invitrogen). The NL20 human bronchial epithelial cell line was supplied from ATCC (NCI-PBCF-CRL2503) and grown in F12-K media supplemented with 4% v/v FBS and 1% v/v penicillin/streptomycin (Gibco, Invitrogen) alongside additional insulin (0.005 mg/mL), epidermal growth factor (10 ng/mL), transferrin (0.001 mg/mL), and hydrocortisone (500 ng/mL). The stable ACE2/TMPRSS-expressing human embryonic kidney HEK293 cell line was kindly provided by Dr. Marc Johnson lab (University of Missouri School of Medicine) and grown in DMEM media supplemented with 10% v/v FBS and 1% v/v penicillin/streptomycin (Gibco, Invitrogen). All cells were grown in 75 cm^2 cell culture flasks (Falcon, Corning) incubated at 37°C and 5% CO_2 in a humidified Heracell VIOS 160i incubator (ThermoFisher Scientific).

Cell Viability

Cells were seeded onto 96-well flat-bottom, tissue culture-treated plate (Falcon) at a density of 5000 cells/well and incubated for 24 h. The cells were then treated with varying concentrations of ACE2-docking filaments (20:1 molar ratio of Filler:Ligand, in 1×PBS at pH = 7.4), ranging from 0.1 to 100 μM, and then incubated for an additional 48 h. Cell viability was assessed with an MTT assay (Invitrogen) according to the manufacturer's protocols. Experiments were performed with 5 technical repeats for each condition with a total of 3 biological repeats.

In Vivo Imaging System (IVIS) Fluorescence Imaging

To execute the imaging, mice were anesthetized with ketamine/xylazine, and given Cy5.5-loaded filaments through nasal inhalation. 24 hour-post inhalations, mice were sacrificed and their whole lungs were isolated. The lung fluorescence image was performed in the IVIS 100 system for 2-5 min at high sensitivity. Regions of interest was identified and quantified using Living Image software (Caliper).

Supplemental References

1. Woody, R.W. (1974). In Peptides, polypeptides and proteins, E.R. Blout, F.A. Bovey, M. Goodman, and N. Lotan, eds. (John Wiley & Sons, Inc.), pp. 338-348.
2. Brahms, S., Brahms, J., Spach, G., and Brack, A. (1977). Identification of β,β-turns and unordered conformations in polypeptide chains by vacuum ultraviolet circular dichroism. Proceedings of the National Academy of Sciences *74*, 3208-3212. 10.1073/pnas.74.8.3208.
3. Brain, J.D., Knudson, D.E., Sorokin, S.P., and Davis, M.A. (1976). Pulmonary distribution of particles given by intratracheal instillation or by aerosol inhalation. Environmental Research *11*, 13-33. 10.1016/0013-9351(76)90107-9.
4. Silva, R.M., Doudrick, K., Franzi, L.M., TeeSy, C., Anderson, D.S., Wu, Z., Mitra, S., Vu, V., Dutrow, G., Evans, J.E., et al. (2014). Instillation versus Inhalation of Multiwalled Carbon Nanotubes: Exposure-Related Health Effects, Clearance, and the Role of Particle Characteristics. ACS Nano *8*, 8911-8931. 10.1021/nn503887r.
5. Leong, B.K.J., Coombs, J.K., Sabaitis, C.P., Rop, D.A., and Aaron, C.S. (1998). Quantitative morphometric analysis of pulmonary deposition of aerosol particles inhaled via intratracheal nebulization, intratracheal instillation or nose-only inhalation in rats. Journal of Applied Toxicology *18*, 149-160. 10.1002/(SICI)1099-1263(199803/04)18:2<149::AID-JAT490>3.0.CO;2-L.
6. Cheetham, A.G., Zhang, P., Lin, Y.-a., Lock, L.L., and Cui, H. (2013). Supramolecular Nanostructures Formed by Anticancer Drug Assembly. Journal of the American Chemical Society *135*, 2907-2910. 10.1021/ja3115983.
7. Su, H., Wang, F., Wang, Y., Cheetham, A.G., and Cui, H. (2019). Macrocyclization of a Class of Camptothecin Analogues into Tubular Supramolecular Polymers. Journal of the American Chemical Society *141*, 17107-17111. 10.1021/jacs.9b09848.
8. Wang, F., Su, H., Lin, R., Chakroun, R.W., Monroe, M.K., Wang, Z., Porter, M., and Cui, H. (2020). Supramolecular Tubustecan Hydrogel as Chemotherapeutic Carrier to Improve Tumor Penetration and Local Treatment Efficacy. ACS Nano *14*, 10083-10094. 10.1021/acsnano.0c03286.
9. Tantakitti, F., Boekhoven, J., Wang, X., Kazantsev, R.V., Yu, T., Li, J., Zhuang, E., Zandi, R., Ortony, J.H., Newcomb, C.J., et al. (2016). Energy landscapes and functions of supramolecular systems. Nature Materials *15*, 469-476. 10.1038/nmat4538.
10. Chen, C.H., Palmer, L.C., and Stupp, S.I. (2018). Self-Repair of Structure and Bioactivity in a Supramolecular Nanostructure. Nano Letters *18*, 6832-6841. 10.1021/acs.nanolett.8b02709.